NORDITA,

STOCKHOLM UNIVERSITY

Chaotic dynamics of an elastic filament in periodically driven Stokes flow

---

Author:
Vipin Agrawal

Supervisor:
Dr. Dhrubaditya Mitra
Dr. Supriya Krishnamurthy

Abstract

We use direct numerical simulations to solve for a filament (with bending modulus B, length L), suspendend in the fluid (with dynamic viscosity η), obeying Stokesian dynamics in a linear shear flow whose strain rate $\dot{\gamma}$ is a periodic function of time(t), $\dot{\gamma} = S\sin(\omega t)$. The dynamical behaviour is determined by the elasto-viscous number, $\overline{\mu} \equiv (8\pi\eta S L^4)/B$ and $\sigma = \omega/S$. For a fixed σ, for small enough μ, the filament remains straight; as $\overline{\mu}$ increases we observe respectively buckling, breakdown of time-periodicity and appearance of two-period and eventually complex spatiotemporal solutions. To analyze the dynamics of this non-autonomous system we consider the map obtained by integrating the dynamical equations over exactly one period. We find that this map has multiple fixed points and periodic orbits for large enough μ. For μ and σ within a certain range we find qualitative evidence of mixing of passive tracers.

Sammanfattning på svenska

Contents

List of Figures

List of Tables

Reading book after book the whole world died,
and none ever became learned!
But understanding the root matter is
what made them gain the knowledge!
– Kabir Granthavali, XXXIII.3,
Translated by Charlotte Vaudeville

Chapter 1

Introduction

The understanding of the dynamics of soft elastic bodies in viscous fluid is important from both fundamental and application-oriented points of view.

Dynamics of viscous fluids is determined by the Reynolds number – $\mathrm{Re} = LU/\nu$ where L is the typical length-scale, U the typical velocity scale and ν the dynamic viscosity of the fluid. For example, a bacterial swimming corresponds to a Reynolds number of 10^{-5}, whereas a flying bird has a Reynolds number of about 10^4, see fig 1.1. At small Reynolds number, the inertial, nonlinear term of the Navier–Stokes equation can be ignored. Such flows are called Stokes flows. Many biophysical phenomena are well described by the Stokes flows e.g. swimming of unicellular organism such as Chlamydomonas to multicellular organisms Volvox [1], flow of human blood in capillaries [2], beating of flagella [3, 4] etc. Furthermore the subject of microfluidics almost entirely (except inertial microfluidics [5]) belongs to Stokes flows. In this regime, the flows obey linear equations and they are also time-reversible [6]. Consequently, such flows are non-mixing. Is it possible to generate mixing in Stokes flows by clever stirring strategies? This is a very well-studied [7] but open question at this moment. If the flow is stirred by a periodic stirrer, mixing is impossible [8] because after one period of stirring all the variables of the problem returns to their initial values. This suggests that for effective mixing, the stirrer must never repeat itself – one possibility is that the motion of the stirrer is chaotic. A necessary condition for chaos is nonlinear dynamics. In the absence of nonlinearity in the flow, we are left with the choice of a stirrer whose dynamics is nonlinear. This is possible if the elastic behavior of the stirrer is nonlinear. In elasticity of solids, the dynamical variable is the displacement of a point from its undeformed position. If this displacement is small and the stress-strain response (constitutive relation) of the body is linear – which is true for most solid materials except e.g, foams – elasticity is a linear problem [9]. But if the displacement is large then even for linear constitutive relation the elastic response can be nonlinear (see appendix A for a discussion on non-linearity of elastica). Canonical examples of such problems are two-dimensional membranes or shells in three dimensional space or one dimensional rods in two or three dimensional space (see chapter 1 of [9], chapter 2 of [10]). Hence it seems plausible that an easily deformable but periodically driven filament can give rise to complex dynamical behaviour which never repeats itself, consequently can act as a stirrer to mix flows at very small Reynolds number. We explore this fundamental question in this thesis.

From an application-oriented point of view, elastic objects coupled with low-Reynolds number flows have potential application to a wide range of problems in biology. Red blood cells (RBC) get harder due to malaria – studying the interaction of elastic body such as RBC and blood flow could help us in developing new affordable microfluidic devices to detect malaria [11], and separation of biological objects, such as cells and proteins, biological transport in eukaryotic cells [12], dynamics of actin filaments and DNA [13, 14] etc.

The rest of this chapter is organized in the following manner. In section 1.1, we shall give a short summary of the fundamentals of Stokes flows. In section 1.2, we shall summarize the nonlinear elastic behavior of deformable rods. In section 1.3, we establish the machinery for simulating the dynamics of an elastic filament in Stokes flow. In section 1.4, we shall precisely define the problem we are going to study in this thesis.

1.1 Stokes flow: time reversibility and linearity

Motion of an incompressible Newtonian fluid is given by Navier-Stokes equation [15, 16, 17]:

$$\partial_t \boldsymbol{v} + \boldsymbol{v} \cdot \boldsymbol{\nabla} \boldsymbol{v} = -\frac{\boldsymbol{\nabla} p}{\rho} + \nu \nabla^2 \boldsymbol{v} + \boldsymbol{f}_{ex}, \tag{1.1a}$$

$$\boldsymbol{\nabla} \cdot \boldsymbol{v} = 0. \tag{1.1b}$$

Here ρ is constant density of the fluid, $\boldsymbol{v}$ is the velocity, p is the pressure, ν is the kinematic viscosity defined as $\nu \equiv \eta/\rho$, η is the dynamic viscosity and $\boldsymbol{f}_{\text{ex}}$ is the external force e.g. gravity, electro-magnetic forces etc. Equation 1.1a is the equation for momentum conservation and 1.1b is the equation for mass conservation . We take curl of equation 1.1a and write down the vorticity equation:

$$\partial_t \boldsymbol{\varpi} + \boldsymbol{\nabla} \times (\boldsymbol{\varpi} \times \boldsymbol{v}) = \nu \nabla^2 \boldsymbol{\varpi} + \boldsymbol{\nabla} \times \boldsymbol{f}_{\text{ex}}, \tag{1.2}$$

where $\boldsymbol{\varpi} \equiv \boldsymbol{\nabla} \times \boldsymbol{v}$, is vorticity of the fluid. Let us introduce the dimensionless variables:

$$x = \tilde{x} L, \quad \boldsymbol{v} = U \tilde{\boldsymbol{v}}, \quad t = T\tilde{t}, \quad \partial_t = \frac{1}{T}\tilde{\partial}_{\tilde{t}}, \quad \boldsymbol{\nabla} = \frac{1}{L}\tilde{\boldsymbol{\nabla}}, \quad \boldsymbol{f}_{\text{ex}} = F\tilde{\boldsymbol{f}}_{\text{ex}} \tag{1.3}$$

Here L is a length scale, U is a reference velocity scale, and T is a time scale. $\tilde{(\cdot)}$ denotes the dimensionless variables. We write equation 1.2 in non-dimensional form [18]:

$$\frac{1}{\text{St}}\tilde{\partial}_{\tilde{t}} \tilde{\boldsymbol{\varpi}} + \tilde{\boldsymbol{\nabla}} \times (\tilde{\boldsymbol{\varpi}} \times \tilde{\boldsymbol{v}}) = \frac{1}{\text{Re}} \tilde{\nabla}^2 \tilde{\boldsymbol{\varpi}} + F \tilde{\boldsymbol{\nabla}} \times \tilde{\boldsymbol{f}}_{\text{ex}}, \tag{1.4a}$$

$$\tilde{\boldsymbol{\nabla}} \cdot \tilde{\boldsymbol{v}} = 0. \tag{1.4b}$$

We get two dimensionless number

$$\text{Re} = \text{Reynolds number} = \frac{\text{UL}}{\nu}, \qquad \text{St} = \text{Stokes Number} = \frac{\text{UT}}{\text{L}} \tag{1.5}$$

Reynolds number is the ratio between typical inertial and viscous forces, and Stokes number

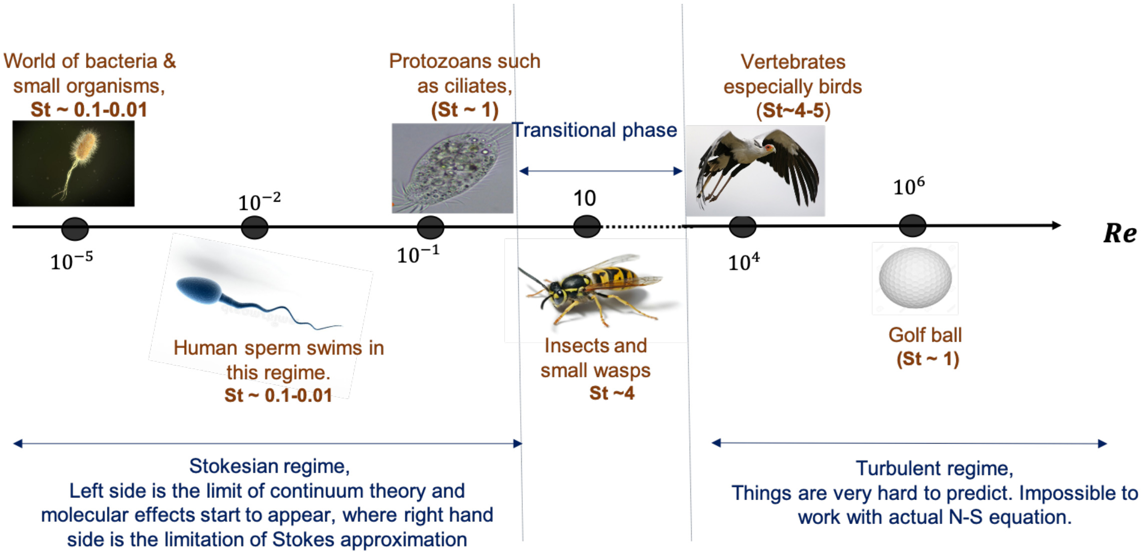

Figure 1.1: Reynolds and Stokes number of various events. Stokes, Eulerian and transitional phase is loosely defined based on Reynolds number. value of $\nu = 10^{-6} m^2/s$ for water, and $\nu = 1.5 \times 10^{-5} m^2/s$ for air is assumed. (fig not to scale)

characterizes the time scale of particles or any foreign body in the flow.

Let us assume that there is no external force or time-scale in the system. Then $T \sim L/U$ or St ~ 1. In that case, dynamics of the fluid flow is determined by only one dimensionless number, Re [18]. We visually represent the importance of Re in figure 1.1. Realm of microfluidics generally deals with the flows with very small characteristic length scale, L, i.e. Re $\ll 1$. We rewrite equation 1.4a:

$$\mathrm{Re}\left[\tilde{\partial}_{\tilde{t}}\tilde{\boldsymbol{\varpi}} + \tilde{\boldsymbol{\nabla}} \times (\tilde{\boldsymbol{\varpi}} \times \tilde{\boldsymbol{v}})\right] = \tilde{\nabla}^2 \tilde{\boldsymbol{\varpi}} \tag{1.6}$$

We take the limit Re $\to 0$ to get:

$$\tilde{\nabla}^2 \tilde{\boldsymbol{\varpi}} = \mathbf{0} \tag{1.7a}$$

$$\Rightarrow \tilde{\nabla}^2 \tilde{\boldsymbol{v}} = \tilde{\boldsymbol{\nabla}} \phi \tag{1.7b}$$

Comparing equation 1.1a, and equation 1.7*b*, we note that the scalar function, ϕ, is proportional to p/η. Hence we write the Stokes equations in dimensional form [18]:

$$\eta \nabla^2 \boldsymbol{v} = \boldsymbol{\nabla} p \qquad \boldsymbol{\nabla} \cdot \boldsymbol{v} = 0 \tag{1.8}$$

The Stokes equations are simpler than the Navier Stokes equation as they do not contain non-linear terms. The equation has two very important features: 1) linearity 2) time independence. These two features are what defines the Stokesian realm. Due to its linearity, Stokes equation has a unique solution for a given boundary conditions [19]. Since there is no time-dependent term as well, the dynamics of the flow is completely determined by the boundary condition specified at that instant i.e. the flow instantly adapts to any change in the boundary condition.

1.1.1 A sphere in Stokes flow

In this section, we first develop the expression for flow disturbances due to a fixed sphere in an ambient flow, $\boldsymbol{v}_\infty(\boldsymbol{X})$ [20]. Second, we calculate the forces and torques required to keep the sphere fixed. Third, we calculate the flow disturbances due to an external force, torque and stresslet in a quiescent flow.

Let us assume the ambient flow, $\boldsymbol{v}_\infty(\boldsymbol{X})$, to be a linear function of space. Then

$$v_\infty^\alpha(\boldsymbol{X}) = v_\infty^\alpha + (\Omega_\infty^{\alpha\beta} + E_\infty^{\alpha\beta})X^\beta \tag{1.9}$$

Where $\Omega_\infty^{\alpha\beta}$ and $E_\infty^{\alpha\beta}$ represent rate of rotation and rate of strain of the ambient flow respectively [20]. Einstein summation is implied. Since the Stokes equations are linear, flow disturbances due to the presence of fixed sphere in the ambient flow are sum of flow disturbances due to the presence of fixed sphere in an ambient flow with translational velocity, rotation, and strain individually. The actual velocity at any Eulerian point $\boldsymbol{X}$, $\boldsymbol{V}_{\text{act}}(\boldsymbol{X})$, satisfies the Stokes equation (1.8). Since the ambient flow is linear i.e. $\nabla^2\boldsymbol{v}_\infty(\boldsymbol{X}) = \boldsymbol{0}$, the flow disturbances, $\boldsymbol{V}(\boldsymbol{X}) = \boldsymbol{V}_{\text{act}}(\boldsymbol{X}) - \boldsymbol{v}_\infty(\boldsymbol{X})$, also satisfies the Stokes equation. To find the flow disturbances, $\boldsymbol{V}(\boldsymbol{X})$, we solve the Stokes equations (1.8) with the following boundary conditions [20]:

$$V^\alpha\left(X = |\boldsymbol{X}| = \frac{d}{2}\right) = -v_\infty^\alpha - \epsilon^{\alpha\beta\gamma}\omega_\infty^\beta X^\gamma - E_\infty^{\alpha\beta}X^\beta \tag{1.10a}$$

$$\boldsymbol{V}\left(X = |\boldsymbol{X}| \to \infty\right) = \boldsymbol{0} \tag{1.10b}$$

$$p\left(X = |\boldsymbol{X}| \to \infty\right) = 0. \tag{1.10c}$$

Here $\omega_\infty^\alpha = -\left(1/2\right)\epsilon^{\alpha\beta\gamma}\Omega^{\beta\gamma}$, and d is the diameter of the sphere. The first, second and third term in the right hand side (RHS) of the equation 1.10a are the contributions from translation, rotation and straining motion respectively. The solution is (see chapter 2 of [20], chapter 2,3 of [19] for the complete derivation):

$$V^\alpha(\boldsymbol{X}) = -\frac{3d}{8}v_\infty^\beta\left(1 + \frac{d^2}{24}\nabla^2\right)\mathcal{G}^{\alpha\beta}(\boldsymbol{X}) - \frac{d^3}{8X^3}\epsilon^{\alpha\beta\gamma}\omega_\infty^\beta X^\gamma + \frac{5d^3}{48}\left(E_\infty^{\beta\gamma}\partial^\gamma\right)\left(1 + \frac{d^2}{24}\nabla^2\right)\mathcal{G}^{\alpha\beta}(\boldsymbol{X}) \tag{1.11a}$$

$$p(\boldsymbol{X}) = -\frac{3\eta d}{2}\frac{v_\infty^\alpha X^\alpha}{X^3} + 0 - \frac{5\eta d^3}{8}\frac{X^\alpha E_\infty^{\alpha\beta}X^\gamma}{X^5} \tag{1.11b}$$

where $\mathcal{G}^{\alpha\beta}(\boldsymbol{X})$ is the Green's function (also known as Stokeslet):

$$\mathcal{G}^{\alpha\beta} = \frac{\delta^{\alpha\beta}}{X} + \frac{X^\alpha X^\beta}{X^3}. \tag{1.12}$$

Note that, the second term in the RHS of the equation 1.11b is 0, to show that there is no pressure disturbance in the flow due to the rotation of the sphere. We compute the hydrodynamic force,F_{h}, on the sphere:

$$F_{\text{h}}^\alpha = \iint_{S_{\text{p}}} \sigma^{\alpha\beta}\hat{n}^\beta dS_{\text{p}}, \tag{1.13}$$

where

$$\sigma^{\alpha\beta} = -p\delta^{\alpha\beta} + \eta\left(\partial^\alpha V^\beta + \partial^\beta V^\alpha\right), \tag{1.14}$$

is the stress on the sphere due to the flow, S_p denote the surface of the sphere and $\hat{\boldsymbol{n}}$ is the unit normal in the outward direction of the surface S_p. Only the translational part of the velocity disturbance (first term in the RHS of the equation 1.11) contributes to the force on the sphere. An equal and opposite force, $\boldsymbol{F}$, is required to hold the sphere fixed i.e. $\boldsymbol{F} = -\boldsymbol{F}_\mathrm{h}$.

$$\boldsymbol{F} = -\boldsymbol{F}_\mathrm{h} = -3\pi\eta d\boldsymbol{v}_\infty \tag{1.15}$$

The rotation and the straining term (second and third term in RHS of the equation 1.11) contributes to the first moment of force distribution which is:

$$\iint_S \sigma^{\alpha\gamma} X^\beta \hat{n}^\gamma dS_\mathrm{p} = \mathcal{A}^{\alpha\beta} + \mathcal{S}^{\alpha\beta}. \tag{1.16}$$

Here $\mathcal{A}^{\alpha\beta}$ and $\mathcal{S}^{\alpha\beta}$ are the antisymmetric and symmetric part of the first moment respectively [20]:

$$\begin{aligned}
\mathcal{A}^{\alpha\beta} &= \frac{1}{2}\iint_S \left[\sigma^{\alpha\gamma}X^\beta - \sigma^{\beta\gamma}X^\alpha\right]\hat{n}^\gamma dS_\mathrm{p} = -\frac{1}{2}\epsilon^{\alpha\beta\gamma}T_\mathrm{h}^\gamma \\
\mathcal{S}^{\alpha\beta} &= \frac{1}{2}\iint_S \left[\sigma^{\alpha\gamma}X^\beta + \sigma^{\beta\gamma}X^\alpha\right]\hat{n}^\gamma dS_\mathrm{p},
\end{aligned} \tag{1.17}$$

where $\boldsymbol{T}_\mathrm{h}$ is the hydrodynamic torque on the sphere. If $\boldsymbol{T}$ is an external torque to hold the sphere fixed, then $\boldsymbol{T} = -\boldsymbol{T}_\mathrm{h}$. By substituting equation 1.14,1.11a in equation 1.17, we get:

$$\begin{aligned}
\boldsymbol{T} = -\boldsymbol{T}_\mathrm{h} &= -\pi\eta d^3\boldsymbol{\omega} \\
\mathcal{S}^{\alpha\beta} &= \frac{5}{6}\pi\eta d^3 E_\infty^{\alpha\beta}.
\end{aligned} \tag{1.18}$$

It is useful to express equation 1.11a in terms of $F^\beta, T^\beta, \mathcal{S}^{\alpha\beta}$:

$$V^\alpha(\boldsymbol{X}) = F^\beta\left(1 + \frac{d^2}{24}\nabla^2\right)\frac{\mathcal{G}^{\alpha\beta}(\boldsymbol{X})}{8\pi\eta} + \frac{1}{8\pi\eta X^3}\epsilon^{\alpha\beta\gamma}T^\beta X^\gamma + \mathcal{S}^{\beta\gamma}\partial^\gamma\left(1 + \frac{d^2}{24}\nabla^2\right)\frac{\mathcal{G}^{\alpha\beta}(\boldsymbol{X})}{8\pi\eta} \tag{1.19}$$

Now, if we imagine an inertialess sphere in a quiescent fluid with external force $\boldsymbol{F}$, external torque $\boldsymbol{T}$, and stresslet $\mathcal{S}^{\alpha\beta}$ such that the motion of the sphere still follows the assumption of the Stokes flow. The fluid flow due to the external $\boldsymbol{F}$,$\boldsymbol{T}$ and $\mathcal{S}^{\alpha\beta}$ on the sphere, is given by equation 1.19 [20].

1.1.2 A sphere in shear flow:

We consider a freely suspended sphere (i.e. the sphere is not under influence of any external force or torque) in shear flow, $\boldsymbol{v}_\infty = (Sy, 0, 0)$. We wish to determine the flow disturbances due to the sphere. For the shear flow, we write:

$$E_\infty^{\alpha\beta} = \begin{bmatrix} 0 & S/2 & 0 \\ S/2 & 0 & 0 \\ 0 & 0 & 0 \end{bmatrix}, \qquad \Omega^{\alpha\beta} = \begin{bmatrix} 0 & S/2 & 0 \\ -S/2 & 0 & 0 \\ 0 & 0 & 0 \end{bmatrix} \tag{1.20}$$

Without any loss of generality, we take the origin of shear flow at the center of the sphere. Hence, the sphere does not have any translational motion. However, the shear flow causes the sphere to rotate with an angular velocity, $\boldsymbol{\omega}$. The Stokes equations (1.8) does not contain inertia. In addition, let us assume that the sphere also does not have any inertia. Then the sphere rotates with the angular velocity of the fluid i.e. $\boldsymbol{\omega} = \boldsymbol{\omega}_\infty = -(1/2)\epsilon^{\alpha\beta\gamma}\Omega^{\beta\gamma}$. Hence, there will not be any disturbances in the flow due to the $\Omega^{\alpha\beta}_\infty$ as there is no relative angular velocity between the fluid and the sphere. Note that, by the same logic, even if the sphere is not at the origin, there are no disturbances in the flow due to translation.

The symmetric part, $E^{\alpha\beta}_\infty$, exerts no net force or torque on the sphere due to its symmetry. The flow disturbance due to $E^{\alpha\beta}_\infty$ (equation 1.11a) is :

$$V^\alpha(\boldsymbol{X}) = \frac{5d^3}{48}\left(E^{\beta\gamma}_\infty \partial^\gamma\right)\left(1 + \frac{d^2}{24}\nabla^2\right)\mathcal{G}^{\alpha\beta}(\boldsymbol{X}) \tag{1.21}$$

1.1.3 Faxén's law

So far, we have assumed the ambient flow to be linear. If the ambient flow is not linear, there is an additional term in the expression for $\boldsymbol{F}$, $\boldsymbol{T}$ and $\mathcal{S}^{\alpha\beta}$, known as Faxén's law [21, 20, 19, 22]:

$$\boldsymbol{F} = 3\pi\eta d\left[\left(1 + \frac{d^2}{24}\nabla^2\right)\boldsymbol{v}_\infty(\boldsymbol{X} = \boldsymbol{0}) - \boldsymbol{U}\right], \tag{1.22a}$$

$$\boldsymbol{T} = \pi\eta d^3\left[\boldsymbol{\omega}_\infty(\boldsymbol{X} = \boldsymbol{0}) - \boldsymbol{W}\right], \tag{1.22b}$$

$$\mathcal{S}^{\alpha\beta} = \frac{5}{6}\pi\eta d^3\left(1 + \frac{d^2}{40}\right)E^{\alpha\beta}_\infty. \tag{1.22c}$$

Here $\boldsymbol{U}$ and $\boldsymbol{W}$ are the velocities and angular velocity of the sphere respectively and we take the center of the sphere to be at the origin.

1.1.4 N spheres in quiescent fluid

Consider N spheres each subject to an external force, $\boldsymbol{F}_i$, where i goes from 0 to N. We do not consider any external torque or external stresslet on the sphere. We assume that the motion of spheres follows the assumption of the Stokes flow. We exploit the linearity of Stokes equations to write [19, 23]:

$$U^\alpha_i = \sum_{i=0}^{i=N}\mathcal{M}^{\alpha\beta}_{ij}F^\beta_j, \tag{1.23}$$

or in the matrix form,

$$\begin{bmatrix} U^\alpha_1 \\ U^\alpha_2 \\ \vdots \\ U^\alpha_N \end{bmatrix} = \begin{bmatrix} \mathcal{M}^{\alpha\beta}_{11} & \mathcal{M}^{\alpha\beta}_{12} & \dots & \mathcal{M}^{\alpha\beta}_{1N} \\ \mathcal{M}^{\alpha\beta}_{21} & \mathcal{M}^{\alpha\beta}_{22} & \ddots & \\ \vdots & \vdots & & \\ \mathcal{M}^{\alpha\beta}_{N1} & \mathcal{M}^{\alpha\beta}_{N2} & \dots & \mathcal{M}^{\alpha\beta}_{NN} \end{bmatrix} \begin{bmatrix} F^\beta_1 \\ F^\beta_2 \\ \vdots \\ F^\beta_N \end{bmatrix}. \tag{1.24}$$

Here $\boldsymbol{U}_i$ is the velocity of the i^{th} sphere, $\mathcal{M}^{\alpha\beta}$ is the mobility tensor. The Greek indices run over coordinates and the Latin indices run over the number of spheres.

An exact closed-form solution to the Stokes equations (1.8) with boundary conditions:

$$\int\int_{S_i} \sigma^{\alpha\beta}(\boldsymbol{X}_i)\hat{n}^{\beta} dS_i = F_i^{\alpha} \quad \text{for} \quad \mathrm{X} \in \mathrm{S_i}, \mathrm{i} = 1, \dots \mathrm{N} \quad , \tag{1.25a}$$

$$\boldsymbol{V}(\boldsymbol{X}_i \to \infty) = 0 \quad , \tag{1.25b}$$

$$p(\boldsymbol{X}_i \to \infty) = 0 \quad , \tag{1.25c}$$

does not exist for $N \geq 2$. So we find the solution by perturbative methods. The perturbation series for $\boldsymbol{U}_i$, is expanded in the powers of $(d/X_{ij} \to 0)$, where d is diameter of all the spheres, $X_{ij} = \left|\boldsymbol{X}_{ij}\right| = \left|\boldsymbol{X}_i - \boldsymbol{X}_j\right|$, and j goes from 0 to N.

For simplicity, let us consider $N = 2$. We start by assuming that the spheres are very far from each other $(d/X) \to 0$, and write the velocity of the spheres using equation 1.15 – this is the zeroth order approximation to the problem. The flow field at any Eulerian point is the sum of flow disturbances due to both spheres i.e. at the lowest order, we neglect the hydrodynamic interaction between them. Next, we consider that the ambient flow around the second sphere consists of flow disturbances (velocity field and stresslet) produced by the first sphere and vice-versa – this generates a correction to the earlier solution for the sphere velocity, and is the first order approximation to the problem. Similarly, we get the higher order terms in the series – this method is known as method of images [24, 23]. We write the final velocity $\boldsymbol{U}_i$ as:

$$\boldsymbol{U}_i = \boldsymbol{U}_i^{(0)} + \boldsymbol{U}_i^{(1)} + \dots , \tag{1.26}$$

where the superscript (m) denotes the m^{th} order approximation.

Zeroth order approximation:

We take $N = 2$. As described earlier, for zeroth order approximation we take $(X_{ij}/d) \to \infty$ i.e. we write the velocity of the sphere using equation 1.15:

$$\boldsymbol{U}_i^{(0)} = \frac{\boldsymbol{F}_i}{3\pi\eta d} \tag{1.27}$$

and the mobility matrix consists of only diagonal terms:

$$\mathcal{M}^{\alpha\beta} = \begin{bmatrix} \frac{1}{3\pi\eta d}\delta^{\alpha\beta} & 0 \\ 0 & \frac{1}{3\pi\eta d}\delta^{\alpha\beta} \end{bmatrix} \tag{1.28}$$

We use equation 1.19 (only the force part, as torque and stresslet is zero) to write the velocity field at any Eulerian point $\boldsymbol{X}$:

$$V^{(0),\alpha}(\boldsymbol{X}) = \sum_{i=1}^{2} V_i^{(0),\alpha} = \sum_{i=1}^{2} F_i^{\beta} \left(1 + \frac{d^2}{24}\nabla^2\right) \frac{\mathcal{G}^{\alpha\beta}(\boldsymbol{X} - \boldsymbol{X}_i)}{8\pi\eta}, \tag{1.29}$$

where $\boldsymbol{V}_i^{(0)}$ is the flow disturbance due to i^{th} sphere.

First order approximation:

We notice that, the zeroth order velocity on each sphere $\boldsymbol{U}_i^{(0)}$, produce exactly the prescribed forces $\boldsymbol{F}_i$. So the next correction in the velocity $\boldsymbol{U}_i$ should be such that, they do not produce any additional forces on the sphere. As described earlier, the flow field generated by the second sphere acts as an ambient flow around the first sphere. We use Faxèn's law (equation 1.22a) to write:

$$\begin{aligned} U_1^{(1),\alpha} &= \left(1 + \frac{d^2}{24}\nabla^2\right) V_2^{(0),\alpha}(\boldsymbol{X}_1) \\ &= \frac{3d}{8}\boldsymbol{U}_2^{(0),\beta}\left(1 + \frac{d^2}{12}\nabla^2 + \frac{d^4}{496}\nabla^4\right)\mathcal{G}^{\alpha\beta}(\boldsymbol{X}_1 - \boldsymbol{X}_2) \end{aligned} \tag{1.30a}$$

$$\mathcal{S}_1^{(1),\alpha\beta} = \frac{5}{6}\pi\eta d^3\left(1 + \frac{d^2}{40}\nabla^2\right)E_2^{(0),\alpha\beta}(\boldsymbol{X} = \boldsymbol{X}_1). \tag{1.30b}$$

Here $E_i^{\alpha\beta} = (1/2)[\partial^\alpha V_i^\beta + \partial^\beta V_i^\alpha]$. Similarly, the expression for $\boldsymbol{U}_2$ and $\mathcal{S}_2^{\alpha\beta}$ is also written.

The final velocity of i^{th} sphere $\boldsymbol{U}_i$ is the sum of zeroth order and first order velocities. We write the final mobilty matrix for N spheres:

$$\mathcal{M}_{ij}^{\alpha\beta}(\boldsymbol{X}_{ij}) = \left\{\begin{array}{ll} \frac{1}{8\pi\eta X_{ij}}\left[\delta^{\alpha\beta} + \frac{X_{ij}^\alpha X_{ij}^\beta}{X_{ij}^2} + \frac{d^2}{2X_{ij}^2}\left(\frac{\delta^{\alpha\beta}}{3} - \frac{X_{ij}^\alpha X_{ij}^\beta}{X_{ij}^2}\right) + O\left(\frac{d^4}{X_{ij}^4}\right)\right] & , i \neq j \\ \frac{1}{3\pi\eta d}\delta^{\alpha\beta} & , i = j \end{array}\right\}. \tag{1.31}$$

Here $i, j = \{0, 1, \ldots, N\}$, and $X_{ij} = \left|\boldsymbol{X}_{ij}\right| = \left|\boldsymbol{X}_i - \boldsymbol{X}_j\right|$. Equation 1.31 is known as Rotne-Pragor tensor [25, 26]. The velocity field at an Eulerian point $\boldsymbol{X}$, upto first order approximation is:

$$\begin{aligned} V^\alpha(\boldsymbol{X}) &= \sum_{i=1}^{N}\left[F_i^\beta\left(1 + \frac{d^2}{24}\nabla^2\right)\frac{\mathcal{G}^{\alpha\beta}(\boldsymbol{X} - \boldsymbol{X}_i)}{8\pi\eta} + \frac{5}{6}\pi d^3 E_i^{(0),\beta\gamma}\partial^\gamma\left(1 + \frac{d^2}{40}\nabla^2\right)\frac{\mathcal{G}^{\alpha\beta}(\boldsymbol{X} - \boldsymbol{X}_i)}{8\pi\eta}\right], \\ &= \frac{1}{8\pi\eta X}\left[\delta^{\alpha\beta} + \frac{X^\alpha X^\beta}{X^2} + \frac{d^2}{4X^2}\left(\frac{\delta^{\alpha\beta}}{3} - \frac{X^\alpha X^\beta}{R^2}\right) + O\left(\left(\frac{d}{X}\right)^3\right)\right] \end{aligned} \tag{1.32}$$

Note that, the first order correction to the sphere velocity, $\boldsymbol{U}_i^{(1)}$ does not have any contribution to the velocity field, as they do not produce any net force. Though $\mathcal{S}_1^{(1),\alpha\beta}, \mathcal{S}_2^{(1),\alpha\beta}$ has contributions to equation 1.32 but these terms drops faster than $O(d^4/X_{ij}^4)$.

1.1.5 N spheres in shear flow

Let us now consider N spheres in shear flow, $\boldsymbol{v}_\infty$:

$$\boldsymbol{v}_\infty = (Sy, 0, 0) \tag{1.33}$$

with force $\boldsymbol{F}_i$ on i^{th} particle, where $i = \{0 \dots N\}$, and S is the shear rate. The shear flow imposes velocity, angular velocity and stresslet on all the spheres as described in section 1.1.2. There is no external torque on any sphere, so there is no flow disturbance due to the angular motion of the spheres as there is no relative angular velocity between ambient fluid and the sphere. We write the velocity of the spheres, $\boldsymbol{U}_i$ and stresslet around it, $\mathcal{S}_i^{\alpha\beta}$ as:

$$U_i^\alpha = v_\infty^\alpha(\boldsymbol{X}_i) + \sum_{j=0}^{i=N} \left(\mathcal{M}_{ij}^{\alpha\beta} F_j^\beta + \mathcal{N}_{ij}^{\alpha\beta\gamma} E_\infty^{\beta\gamma}(\boldsymbol{X}_j) \right) \tag{1.34}$$

We use the same technique as described in section 1.1.4.

Zeroth order interaction:

For simplicity, we first consider $N = 2$. Velocity and stresslets at the zeroth order approximation are:

$$\begin{aligned} U_i^{(0),\alpha} &= v_\infty^\alpha(\boldsymbol{X}_i) + \frac{\boldsymbol{F}_i}{3\pi\eta d} \\ \mathcal{S}_i^{(0),\alpha\beta} &= \frac{5}{6}\pi\eta d^3 E_\infty^{\alpha\beta}(\boldsymbol{X}_i) \end{aligned} \tag{1.35}$$

In the case of shear flow, the velocity field, $\boldsymbol{V}^{(0)}(\boldsymbol{X})$ at the zeroth order approximation has an additional term than the quiescent fluid (equation 1.29) due to the presence of $\mathcal{S}^{(0),\alpha\beta}$:

$$V^{(0),\alpha}(\boldsymbol{X}) = \sum_{i=1}^{2} \left[F_i^\beta \left(1 + \frac{d^2}{24}\nabla^2\right) + \frac{5}{6}\pi d^3 E_i^{\beta\gamma} \partial^\gamma \left(1 + \frac{d^2}{40}\nabla^2\right) \right] \frac{\mathcal{G}^{\alpha\beta}(\boldsymbol{X} - \boldsymbol{X}_i)}{8\pi\eta} \tag{1.36}$$

First order interaction:

$$\begin{aligned} \boldsymbol{U}_1^{(1),\alpha} &= \left(1 + \frac{d^2}{24}\nabla^2\right) V_2^{(0),\alpha}(\boldsymbol{X}_1) \\ \mathcal{S}_1^{(1),\alpha\beta} &= \frac{5}{6}\pi\eta d^3 \left(1 + \frac{d^2}{40}\nabla^2\right) E_2^{\alpha\beta}(\boldsymbol{X}_1) \end{aligned} \tag{1.37}$$

Similarly, we write expressions for the other sphere i.e. $\boldsymbol{U}_2^{(1),\alpha}$ and $\mathcal{S}_2^{(1),\alpha\beta}$. Upto, the first order approximation, the expression for $\mathcal{M}^{\alpha\beta}$ remains same as in quiescent fluid (equation 1.31). $\mathcal{N}^{\alpha\beta\gamma}$ is:

$$\mathcal{N}_{ij}^{\alpha\beta\gamma}(\boldsymbol{X}_{ij}) = \left\{ \begin{array}{ll} -\frac{5d^3}{16}\frac{X_{ij}^\alpha X_{ij}^\beta X_{ij}^\gamma}{X_{ij}^5} - \frac{d^5}{64}\left[\frac{\delta^{\alpha\beta}X_{ij}^\gamma + \delta^{\alpha\gamma}X_{ij}^\beta}{X_{ij}^5} - \frac{5X_{ij}^\alpha X_{ij}^\beta X_{ij}^\gamma}{X_{ij}^7}\right] & , i \neq j \\ 0 & , i = j \end{array} \right\}. \tag{1.38}$$

Here $i, j = \{0, 1 \dots N\}$ The leading order term in $\mathcal{N}_{ij}^{\alpha\beta\gamma}$ drops as $O(d^3/X_{ij}^2)$.

1.2 Filaments

In elasticity of solids, the dynamical variable is the displacement of a point from its undeformed position. If this displacement is small and the stress-strain response (constitutive relation) of the body is linear [9] – which is true for most solid materials except e.g, foams – elasticity is a linear problem [9]. But if the displacement is large then even for linear constitutive relation, the elastic response can be nonlinear (see appendix A for the discussion on non-linearity of elastica). Canonical examples of such problems are two-dimensional membranes or shells in three-dimensional space or one-dimensional filaments in two or three-dimensional space (see chapter 1 of [9],chapter 2 of [10]).

1.2.1 Kinematics

We first consider a thin filament, i.e. the cross-sectional area of the filament is almost zero, such that it can be represented as a curve. Later, we shall consider a filament with thickness. Let us represent the curve as $\boldsymbol{R}(\xi)$, here $\boldsymbol{R}(\xi)$ is the coordinate of every point on curve embedded in 3 dimension, with parameter ξ in some interval $\mathcal{I}$. We consider only smooth curves i.e. $\frac{d\boldsymbol{R}(\xi)}{d\xi}$ is well defined everywhere in $\mathcal{I}$. The length of such a curve between parameter values ξ_0 and ξ can be defined as:

$$s \equiv \sigma(\xi) = \int_{\xi_0}^{\xi} \left\| \frac{d\boldsymbol{R}(\xi')}{d\xi'} \right\| d\xi \tag{1.39}$$

Where $\|\cdot\|$ denotes the norm. $s = \sigma(\xi)$ is the arc-length of the curve from ξ_0 to ξ.

Since $\sigma(\xi)$ is always an increasing function , we can take its inverse and write $\xi = \sigma^{-1}(s)$. We re-parametrize the curve as $\boldsymbol{R}(\sigma^{-1}(s))$ with respect to arc-length s. Let us derive the relation between both notations for describing a curve. Distance between two nearby points on the curve is given by the Pythagorean theorem:

$$ds^2 = \frac{d\boldsymbol{R}(s)}{d\xi} \cdot \frac{d\boldsymbol{R}(s)}{d\xi} d\xi^2 \qquad \Longrightarrow \qquad \frac{ds}{d\xi} = \left\| \frac{d\boldsymbol{R}(s)}{d\xi} \right\| \tag{1.40}$$

We use this relation to write:

$$\boldsymbol{R}'(s) \equiv \frac{d\boldsymbol{R}(s)}{ds} = \frac{d\boldsymbol{R}(\xi)}{d\xi} \frac{d\xi}{ds} = \frac{d\boldsymbol{R}(\xi)/d\xi}{\|d\boldsymbol{R}(\xi)/d\xi\|} \equiv \widehat{\boldsymbol{T}}(s) \tag{1.41}$$

We denote $(\cdot)'$ as the derivative with respect to s and $\widehat{\boldsymbol{T}}$ denotes the unit tangent vector at every point on the curve.

Intrinsic description of the curve: Frenet-Serret frame

So far, we have described the curve from an extrinsic point of view i.e. we write the coordinate of every point on the curve in three-dimensional coordinate system. The curve is a one-dimensional body embedded in three-dimensional space, so it is useful to describe its kinematics without resorting to any external co-ordinate system – this is called an intrinsic view of the curve. We describe the curve in the frame of unit tangent vector ($\widehat{\boldsymbol{T}}$), unit normal vector($\widehat{\boldsymbol{N}}$) and unit binormal vector ($\widehat{\boldsymbol{B}}$) – this is known as Frenet-Serret frame (as shown in figure 1.2a). These form an orthogonal coordinate system (figure 1.2a):

$$\widehat{\boldsymbol{B}}(s) = \widehat{\boldsymbol{T}}(s) \times \widehat{\boldsymbol{N}}(s) \tag{1.42}$$

We defined $\widehat{\boldsymbol{T}}$ in equation 1.41 and $\widehat{\boldsymbol{N}}$ is a vector perpendicular to $\widehat{\boldsymbol{T}}$. Notice that, if a curve is embedded in three dimension, we have infinite vectors perpendicular to $\widehat{\boldsymbol{T}}$. We choose one of them as a normal vector, which also fixes $\widehat{\boldsymbol{B}}$.

Frenet-Serret frame moves along the curve, from $s = 0$ to $s = L$, as shown in figure 1.2a. The frame for any two nearby points differ by a small rotation $\Delta\boldsymbol{\phi}$:

$$\widehat{\boldsymbol{T}}|_{s+\Delta s} = \widehat{\boldsymbol{T}}|_s + \boldsymbol{\Delta\phi} \times \widehat{\boldsymbol{T}}|_s \qquad \Longrightarrow \qquad \widehat{\boldsymbol{T}}'(s) = \frac{d\boldsymbol{\phi(s)}}{ds} \times \widehat{\boldsymbol{T}}(s). \tag{1.43}$$

We can write the similar equations for $\widehat{\boldsymbol{N}}$ and $\widehat{\boldsymbol{B}}$. Equation 1.43 tells us that the $\widehat{\boldsymbol{T}}'\widehat{\boldsymbol{N}}'\widehat{\boldsymbol{B}}'$ is perpendicular to $\widehat{\boldsymbol{T}}\widehat{\boldsymbol{N}}\widehat{\boldsymbol{B}}$. So we choose $\widehat{\boldsymbol{N}}$ in the direction of $\widehat{\boldsymbol{T}}'$:

$$\widehat{\boldsymbol{N}} = \frac{\widehat{\boldsymbol{T}}'(s)}{\left\|\widehat{\boldsymbol{T}}'(s)\right\|} \tag{1.44a}$$

$$\widehat{\boldsymbol{T}}' = \left\|\widehat{\boldsymbol{T}}'(s)\right\| \widehat{\boldsymbol{N}} = \left\|\frac{d^2\boldsymbol{R}(s)}{ds^2}\right\| \widehat{\boldsymbol{N}} \equiv \kappa \widehat{\boldsymbol{N}} \tag{1.44b}$$

Here $\kappa(s)$ is curvature of the curve.

Now we derive the same relation for $\widehat{\boldsymbol{N}}'$ and $\widehat{\boldsymbol{B}}'$. Using 1.43 and equation 1.42, we derive [28]:

$$\widehat{\boldsymbol{N}}' = \tau\widehat{\boldsymbol{B}} - \kappa\widehat{\boldsymbol{T}} \tag{1.45a}$$

$$\widehat{\boldsymbol{B}}' = -\tau\widehat{\boldsymbol{N}} \tag{1.45b}$$

Where τ is depicted as torsion of the curve. Equation 1.45 and 1.44 are called the Frenet-Serret frame of equations [27]. Intuitively, the curvature (κ) measures the deflection of the curve from a straight-line and torsion (τ) measures the failure of a curve to be planer[27].

Filaments with thickness: Darboux frame

Frenet-Serret frame describes the kinematics of a curve i.e. a thin elastic filament, although practical filaments have a finite thickness. To describe the filaments in more accurate way, we define the orthonormal frame, $\hat{\boldsymbol{d}}_1$ $\hat{\boldsymbol{d}}_2$ $\hat{\boldsymbol{d}}_3$, moving along the filament, as shown in figure 1.2b. We denote the centerline of the filament as $\boldsymbol{R}(s)$ and the unit tangent vector to the centerline

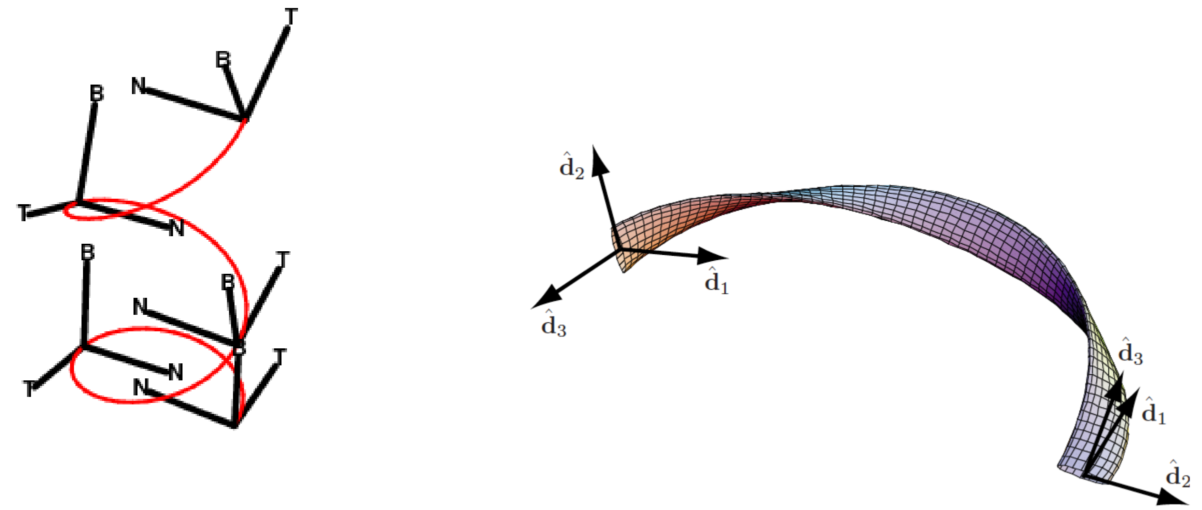

(a) The Frenet-Serret ($\widehat{\boldsymbol{T}}\widehat{\boldsymbol{N}}\widehat{\boldsymbol{B}}$) frame moving along a helix.

(b) Orientation of the fialment in orthonormal frame – $\hat{\boldsymbol{d}}_1$, $\hat{\boldsymbol{d}}_2$ and $\hat{\boldsymbol{d}}_3$ is shown. The figure is reprinted with permission published by Powers [27].

is denoted as $\widehat{\boldsymbol{T}} = \boldsymbol{R}'(s)$. Without any loss of generality, we take $\hat{\boldsymbol{d}}_3 = \widehat{\boldsymbol{T}}$ and $\hat{\boldsymbol{d}}_1$ is chosen arbitrarily in the cross-section perpendicular to the tangent vector, this determines the third axis $\hat{\boldsymbol{d}}_2 = \hat{\boldsymbol{d}}_3 \times \hat{\boldsymbol{d}}_1$ – this is called Darboux frame [10] (figure 1.2b). $\hat{\boldsymbol{d}}_a$ (a=1,2,3) for two nearby points differ by a small rotation and we write:

$$\hat{\boldsymbol{d}}'_a = \boldsymbol{\Omega} \times \hat{\boldsymbol{d}}_a \qquad (\mathrm{a} = 1, 2, 3) \tag{1.46a}$$

where $\boldsymbol{\Omega} = \frac{d\boldsymbol{\phi}}{dt}$ is the rotation rate of the Darboux frame. It is called the Darboux vector [10] and given as: $\boldsymbol{\Omega} = \Omega_1\hat{\boldsymbol{d}}_1 + \Omega_2\hat{\boldsymbol{d}}_2 + \Omega_3\hat{\boldsymbol{d}}_3$.

$$\Omega_1 = \hat{\boldsymbol{d}}'_2 \cdot \hat{\boldsymbol{d}}_3 \tag{1.46b}$$

Similarly, we write equations for Ω_2 and Ω_3.

Darboux vector, $\boldsymbol{\Omega}$, shows the rate at which the Darboux frame rotates when we follow the centerline with unit speed. Ω_1 and Ω_2 are the rotation rate of Darboux frame about $\hat{\boldsymbol{d}}_1$ and $\hat{\boldsymbol{d}}_2$ respectively – they are called material curvatures. Similarly, Ω_3 defines the rotation rate of the frame with respect to $\hat{\boldsymbol{d}}_3$ – it is called the material twist of the filament. The components of $\boldsymbol{\Omega}$ – Ω_1,Ω_2,Ω_3 are shown in figure 1.3. Note that, Darboux frame is different from Frenet-Serret frame which is described in equations 1.44,1.45. Likewise, the material curvature (Ω_1, Ω_2) and twist (Ω_3) is different from κ and τ respectively.

Next, we describe relation between Darboux frame rotation rate (Ω_1,Ω_2,Ω_3) and Frenet-Serret frame rotation rate (κ,τ). Using equation 1.46, 1.44 and 1.45, we write:

$$\Omega_1^2(s) + \Omega_2^2(s) = \kappa^2(s) \tag{1.47}$$

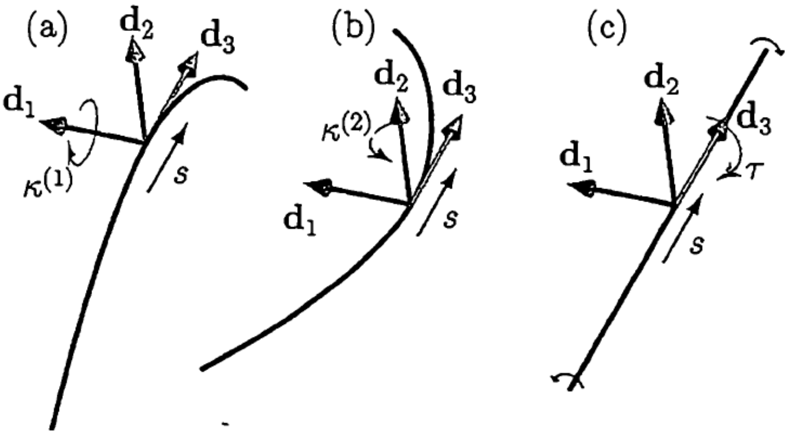

Figure 1.3: Three different type of deformation rate of a filament along the arc-length coordinate is shown. **(a)** Material curvature, Ω_1, which is the frame rotation rate about $\hat{\boldsymbol{d}}_1$. **(b)** Material curvature, Ω_2, which is the frame rotation rate about $\hat{\boldsymbol{d}}_2$. **(c)** Twist of the filament, Ω_3, which is the frame rotation rate about $\hat{\boldsymbol{d}}_3$. Figure adapted and re-printed with permission from [10]

1.2.2 Energy

Energy per unit length ($e(s)$) integrated over whole length gives the total elastic energy of the filament ($\mathcal{H}$). The $e(s)$, for an elastic filament has contributions due to bending i.e. Ω_1 and Ω_2 and twisting i.e. Ω_3 – For the current work, we ignore the twisting of the filament. The energy is a quadratic function of the deformation, i.e. a function of Ω_1, Ω_2[9, 10, 27, 29].

$$e(s) = \frac{YI_{11}}{2}\Omega_1^2(s) + \frac{YI_{22}}{2}\Omega_2^2(s) \tag{1.48a}$$

$$\mathcal{H}^B = \int_{s=0}^{L} e(s)\ ds \tag{1.48b}$$

where Y (unit: Pa = Kg m^{-1} s^{-2}) is the Young's modulus of the filament. I_{11} and I_{22} are the second moment of inertia along the principal axes of inertia of the cross-section of the filament.

For a filament with circular cross-section, $I_{11} = I_{22} = I = \frac{\pi r^4}{4}$. We define $B = YI$, as the bending rigidity of the filament, since this is the contribution due to bending of the filament. Equation 1.48 and 1.47 yields:

$$e(s) = \frac{YI}{2}\left(\Omega_1^2(s) + \Omega_2^2(s)\right) \quad = \quad \frac{B}{2}\kappa^2(s) \tag{1.49a}$$

$$\mathcal{H}^{\mathrm{B}} = \frac{B}{2}\int_{s=0}^{L} \kappa^2(s) ds \tag{1.49b}$$

1.3 Filaments in Stokes flow

We now want to derive the dynamical equations of a filament immersed in a fluid. To do this we must solve the equation of the flow and the filament together with proper boundary conditions for the flow far away from the filament, the boundary condition for the filament and the no-slip boundary condition for the flow at the surface of the filament. In the subsequent sections 1.3.1,1.3.2, we prepare the machinery to describe the dynamics of fluid-filament interaction by an approximate model – the bead-spring model. In the section 1.3.3, we describe the bead-spring model and the numerical algorithm, we use.

First, it is useful to start with a simple model. We consider a harmonic oscillator immersed in a fluid. We further consider the oscillator to move so slowly such that the drag from the fluid is well approximated by the Stokes drag. This is given as (see chapter 7 of [30]):

$$m\ddot{x} + \alpha\dot{x} + kx = f \tag{1.50}$$

where $\dot{()}$ is the derivative with respect to time, m is mass of the particle, α is the friction coefficient, k is the spring constant. First term, $m\ddot{x}$, in equation 1.50 represents inertial effects, $\alpha\dot{x}$ is dissipation in the system, f is an external fore and kx is the conservative force.

1.3.1 Overdamped harmonic oscillator

Consider setting up $\alpha = 0$ in equation 1.50, the system performs oscillatory motion infinitely for some initial perturbation from equilibrium position – This is an undamped state of the system. For $\alpha \neq 0$, oscillation in the system gradually decays towards zero amplitude or attenuate. Equation 1.50 also reads as:

$$\ddot{x} + \omega_0^2 x + 2\omega_0\zeta\dot{x} = \frac{f}{m} \tag{1.51}$$

where $\omega_0^2 = k/m$, $\zeta = \frac{\alpha}{2\sqrt{km}}$ is the damping ratio of the system. For this system, we take ζ to be always positive – which is a fair assumption for a particle in viscous flow. Let us not worry about external force, and consider an ansatz $x = \exp(\mathrm{i}\omega t)$ which is put in equation 1.51 to give the following relation [30]:

$$-\omega^2 + \omega_0^2 + 2\mathrm{i}\zeta\omega_0\omega = 0 \tag{1.52}$$

with solutions

$$\omega = \omega_0\left(\mathrm{i}\zeta \pm \sqrt{1-\zeta^2}\right) = \omega_0\mathrm{i}\zeta \pm \omega_1 \tag{1.53}$$

If the system has damping ratio $\zeta < 1$, ω_1 is real and the system oscillates with frequency ω_1 but the amplitude of oscillation decays to zero – this is called an underdamped oscillator. If $\zeta > 1$, ω_1 is imaginary, the system does not oscillates but decays exponentially – this is called an overdamped oscillator. If $\zeta = 1$, the equation 1.52 has two repeated roots, the system decays exponentially as well in this case but faster than the overdamped case [30, 31].

For a particle in fluid, $\zeta \sim \frac{\eta}{\sqrt{k\rho d}}$ and if we consider the d to be very small, $\zeta \gg 1$ which is a reasonable assumption. For the overdamped case, the inverse decay times (inverse of frequency) are:

$$\tau_f^{-1} = \omega_0 \left(\zeta + \sqrt{\zeta^2 - 1}\right) \xrightarrow{\zeta \gg 1} 2\omega_0 \zeta = \frac{\alpha}{m} \tag{1.54a}$$

$$\tau_s^{-1} = \omega_0 \left(\zeta - \sqrt{\zeta^2 - 1}\right) \xrightarrow{\zeta \gg 1} \frac{1}{2\zeta} = \frac{k}{\alpha} \tag{1.54b}$$

If $\zeta \gg 1$, the fast decay time, τ_f is very small as compared to the slow time decay, τ_s. Thus, for this limit, for long times compared to τ_f, this mode can be ignored. This is also same as neglecting the mass term in the equation 1.50, 1.51.

$$\alpha \dot{x} = -kx \tag{1.55a}$$

$$\dot{x} = -\frac{k}{\alpha} x = -\mu \frac{\partial \mathcal{H}_T}{\partial x} \tag{1.55b}$$

where $\mu = \alpha^{-1}$ is the total dissipation in the system from various sources, $\mathcal{H}_T$ is the total energy of the system.

1.3.2 Is it easier to bend or stretch the filament?

Under typical circumstances, a filament is easier to bend than stretch. Let us consider a filament in Stokes flow i.e. viscous forces are the dominant forces on the filament which balances the bending and stretching forces on the filament. The viscous force, $\boldsymbol{F}^{\mathrm{vis}}$, scales as (equation 1.15):

$$F^{\mathrm{vis}} \sim \eta U_0 L, \tag{1.56}$$

where η is viscosity, U_0 is some velocity scale, L is size of the object. The bending and stretching forces scale as:

$$F^{\mathrm{B}} = -\frac{\delta \mathcal{H}^{\mathrm{B}}(R'')}{\delta R} \sim Y \frac{d^4}{L^2} \quad , \tag{1.57a}$$

$$F^{\mathrm{S}} \sim Y d^2 \quad , \tag{1.57b}$$

where superscripts B, S are for bending and stretching respectively, d is diameter of the filament, L is length of the filament, $B = YI$, Y is the Young's modulus of the material and I is second moment of inertia of the filament i.e. $I \sim d^4$. The bending and stretching force (equation 1.57) balances the viscous forces (equation 1.56). We compute the relaxation time for bending and stretching:

$$\eta U_0 L = Y \frac{d^4}{L^2} \quad \Rightarrow \quad \tau^{\mathrm{B}} = \frac{L}{U_0} = \frac{\eta}{Y} \left(\frac{L}{d}\right)^4 \quad , \tag{1.58a}$$

$$\eta U_0 L = Y d^2 \quad \Rightarrow \quad \tau_{\mathrm{S}} = \frac{\eta}{Y} \left(\frac{L}{d}\right)^2 \quad , \tag{1.58b}$$

$$\frac{\tau^{\mathrm{S}}}{\tau^{\mathrm{B}}} = \left(\frac{d}{L}\right)^2 \lll 1 \quad . \tag{1.58c}$$

Here τ is the relaxation time. We compare the relaxation time for stretching and bending in equation 1.58c and we observe the ratio to be much smaller than 1 as we generally deal with the filaments with very high aspect ratio ($L/d \gg 1$). Therefore, we say that the modulation in the extension relax much faster than the bending deformations for the filament in Stokes flow [27]. Hence, we consider the filament to be almost inextensible throughout the study.

Note that, if the inertial forces are dominant instead of viscous force i.e. $F \sim \rho U_0^2 L^2$, the ratio of stretch and bend timescales is proportional to $d/L \ll 1$ instead of d^2/L^2. Although the ratio of timescales in the case, where inertial forces are dominant, is smaller than the case, where viscous forces are dominant, the assumption that the filament is easier to bend than stretch still holds.

1.3.3 Model

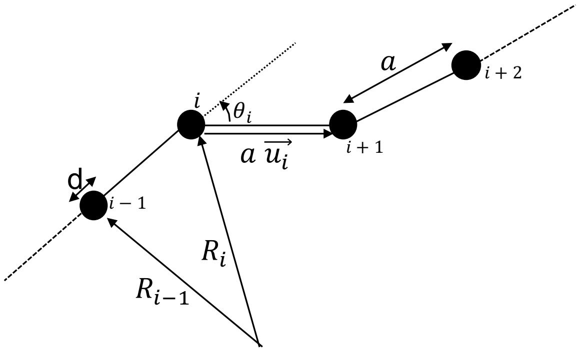

Figure 1.4: Schematic of a freely jointed bead-rod chain. We show $a > d$ for illustration, but we use $a = d$ for our simulation.

We use the bead-spring model to simulate the dynamics of the filament. The model consists of N spherical beads of diameter d, connected by overdamped springs of equilibrium length a, see Figure. 1.4. The position of the center of the i-th bead is $\boldsymbol{R}_i$, where $i = 1, \dots N$. The equation of motion for the i-th bead is given by [26, 32]:

$$\begin{aligned} \partial_t R_{\mathrm{i}}^{\alpha} &= \sum_{j=0}^{N-1} \left[-\mathcal{M}_{\mathrm{ij}}^{\alpha\beta}(\boldsymbol{R}_{ij}) \frac{\delta \mathcal{H}}{\delta R_{\mathrm{j}}^{\beta}} + \mathcal{N}_{ij}^{\alpha\beta\gamma}(\boldsymbol{R}_{ij}) E_{\infty}^{\beta\gamma}(\boldsymbol{R}_{ij}) \right] + v_{\infty}^{\alpha}(\boldsymbol{R}_{\mathrm{i}}) \quad , \\ &= \sum_{j=0}^{N-1} \left[-\frac{1}{8\pi\eta R_{ij}} \left\{ \delta^{\alpha\beta} + \frac{R_{ij}^{\alpha} R_{ij}^{\beta}}{R_{ij}^2} + \frac{d^2}{2R_{ij}^2} \left(\frac{\delta^{\alpha\beta}}{3} - \frac{R_{ij}^{\alpha} R_{ij}^{\beta}}{R_{ij}^2} \right) \right\} \frac{\partial \mathcal{H}}{\partial R_{\mathrm{j}}^{\beta}} \right. \\ & \qquad \left. \frac{1}{N} v_{\infty}^{\alpha}(\boldsymbol{R}_{\mathrm{i}}) - \frac{5d^3}{16} \frac{R_{ij}^{\alpha} R_{ij}^{\beta} R_{ij}^{\gamma}}{R_{ij}^5} E_{\infty}^{\beta\gamma} \right] \quad . \end{aligned} \tag{1.59}$$

Here $\boldsymbol{R}_{\mathrm{i}}$ is the position vector of the center of the i-th bead, $\boldsymbol{R}_{ij} = \boldsymbol{R}_{\mathrm{j}} - \boldsymbol{R}_{\mathrm{i}}$, $\mathcal{H}$ is the elastic Hamiltonian, and $\boldsymbol{v}_{\infty}$ is the velocity of the background flow, $\mathcal{M}^{\alpha\beta}$,$\mathcal{N}^{\alpha\beta\gamma}$ are the hydrodynamic interaction tensors explained in section 1.1.4,1.1.5.

Let us look at the equation 1.59 dimensionally. We compare the terms due to the external shear and flow (terms with $E_{\infty}^{\alpha\beta}, \boldsymbol{v}_{\infty}$), and terms due to elastic forces ($\delta\mathcal{H}/\delta R_{\mathrm{j}}^{\beta}$) separately. We write:

$$\partial_t R_{\mathrm{i}}^{\alpha} \sim \frac{1}{\eta R_{ij}}\left[O(1)+O(1)+O\left(\frac{d^2}{R_{ij}^2}\right)\right]\frac{\delta\mathcal{H}}{\delta R_{\mathrm{j}}^{\beta}} + SX_{ij}\left[O(1)+O\left(\frac{d^3}{R_{ij}^3}\right)\right] \quad . \tag{1.60}$$

In our model, we do not consider the terms of higher order than $O(d^2/R_{ij}^2)$ to obtain:

$$\partial_t R_{\mathrm{i}}^{\alpha} = -\sum_{j=0}^{N-1}\mathcal{M}_{\mathrm{ij}}^{\alpha\beta}(\boldsymbol{R}_{ij})\frac{\delta\mathcal{H}}{\delta R_{\mathrm{j}}^{\beta}} + v_{\infty}^{\alpha}(\boldsymbol{R}_{\mathrm{i}}) \quad , \tag{1.61}$$

The Hamiltonian of the system, $\mathcal{H}$, is $\mathcal{H} = \mathcal{H}^{\mathrm{B}} + \mathcal{H}^{\mathrm{S}}$ – we do not consider twisting. Here $\mathcal{H}^{\mathrm{B}}$ and $\mathcal{H}^{\mathrm{S}}$ are from bending [33, 34]and stretching [26, 35] respectively. The bending energy of a filament for a discrete bead-rod model [36, 34, 33]:

$$\mathcal{H}^{\mathrm{B}} = aB\sum_{i=0}^{N-1}\kappa_i^2 = \frac{B}{a}\sum_{i=0}^{N-1}\hat{\boldsymbol{u}}_i\cdot\hat{\boldsymbol{u}}_{i-1} = \frac{B}{a}\sum_{i=0}^{N-1}\cos\theta_i, \tag{1.62}$$

where

$$\kappa_i = \frac{2}{a}\tan\left(\frac{\theta_i}{2}\right) \approx \frac{\sin(\theta_i)}{a} = \frac{|\hat{\boldsymbol{u}}_{\mathrm{i}}\times\hat{\boldsymbol{u}}_{i-1}|}{a}, \tag{1.63a}$$

$$\hat{\boldsymbol{u}}_{\mathrm{i}} = \frac{\boldsymbol{R}_{i+1}-\boldsymbol{R}_i}{|\boldsymbol{R}_{i+1}-\boldsymbol{R}_i|} \quad , \tag{1.63b}$$

and θ_{i} is the angle between two consecutive unit vectors $\hat{\boldsymbol{u}}_{\mathrm{i}}$ and $\hat{\boldsymbol{u}}_{\mathrm{i}-1}$ (see figure 1.4A). In the second step of equation 1.62, we have dropped a constant term. In the last step of equation 1.63a, we have used small-angle approximation [33]. This is a discrete approximation of contribution to the bending energy (equation 1.48) from curvature.

The stretching energy is: [26, 35]

$$\mathcal{H}^{\mathrm{S}} = \frac{H}{2a}\sum_{\mathrm{i}=0}^{N-1}(|\boldsymbol{R}_{i+1}-\boldsymbol{R}_i| - a)^2, \tag{1.64}$$

where H is the stretching modulus. We ignore thermal fluctuations. Expression for $\delta\mathcal{H}/\delta R_{ij}^{\beta}$ is given in the section 1.3.4. We use the adaptive Runge-Kutta method [37] with cash-karp parameters [38, 39] to evolve the system. We use time-step, Δt, such that

$$\tilde{\Delta} = \frac{B\Delta t}{8\pi\eta\ell^4} = 10^{-11} - 10^{-12} \tag{1.65}$$

We use numerical accuracy of order 10^{-6} [37, 38, 39]. We use CUDA to parallelize the code [1].

---

[1] Our code is available here: https://github.com/dhrubaditya/ElasticString

1.3.4 Discretized bending and stretching force

Total force on any bead is the sum of the bending force and stretching force:

$$\boldsymbol{F} = \boldsymbol{F}^{\mathrm{B}} + \boldsymbol{F}^{\mathrm{S}} = \frac{\partial \mathcal{H}^{\mathrm{B}}}{\partial \boldsymbol{R}_{\mathrm{i}}} + \frac{\partial \mathcal{H}^{\mathrm{S}}}{\partial \boldsymbol{R}_{\mathrm{i}}} = \sum_{i=0}^{N-1} \left[\frac{B}{a} \hat{\boldsymbol{u}}_i \cdot \hat{\boldsymbol{u}}_{i-1} + \frac{H}{2a} \left(|\boldsymbol{R}_{i+1} - \boldsymbol{R}_i| - a \right)^2 \right] \tag{1.66}$$

where $\mathcal{H}^{\mathrm{B}}$ and $\mathcal{H}^{\mathrm{S}}$ is the Hamiltonian for bending and stretching respectively.

Bending force:

$$\boldsymbol{F}_i^{\mathrm{B}} = \frac{B}{a} \left[\frac{\hat{\boldsymbol{u}}_{i-2} + \hat{\boldsymbol{u}}_i}{b_{i-1}} - \frac{\hat{\boldsymbol{u}}_{i+1} + \hat{\boldsymbol{u}}_{i-1}}{b_i} + \left(\hat{\boldsymbol{u}}_i^{\alpha} \hat{\boldsymbol{u}}_{i-1}^{\alpha} + \hat{\boldsymbol{u}}_i^{\alpha} \hat{\boldsymbol{u}}_{i+1}^{\alpha} \right) \left(\frac{\hat{\boldsymbol{u}}_i}{b_i} \right) - \left(\hat{\boldsymbol{u}}_{i-1}^{\alpha} \hat{\boldsymbol{u}}_{i-2}^{\alpha} + \hat{\boldsymbol{u}}_{i-1}^{\alpha} \hat{\boldsymbol{u}}_i^{\alpha} \right) \left(\frac{\hat{\boldsymbol{u}}_{i-1}}{b_{i-1}} \right) \right] \quad i \neq 0, 1, N-1, N-2 \quad . \tag{1.67}$$

The bending force for boundary points are:

$$\boldsymbol{F}_i^{\mathrm{B}} = \frac{B}{a} \left[-\frac{\hat{\boldsymbol{u}}_{i+1}}{b_i} + \left(\hat{\boldsymbol{u}}_i^{\alpha} \hat{\boldsymbol{u}}_{i+1}^{\alpha} \right) \frac{\hat{\boldsymbol{u}}_i}{b_i} \right], \qquad i = 0 \tag{1.68a}$$

$$\boldsymbol{F}_i^{\mathrm{B}} = \frac{B}{a} \left[\frac{\hat{\boldsymbol{u}}_{\mathrm{k}}}{b_{\mathrm{k}-1}} - \frac{\hat{\boldsymbol{u}}_{i+1} + \hat{\boldsymbol{u}}_{i-1}}{b_i} + \left(\hat{\boldsymbol{u}}_i^{\alpha} \hat{\boldsymbol{u}}_{i-1}^{\alpha} + \hat{\boldsymbol{u}}_i^{\alpha} \hat{\boldsymbol{u}}_{i+1}^{\alpha} \right) \left(\frac{\hat{\boldsymbol{u}}_i}{b_i} \right) - \left(\hat{\boldsymbol{u}}_{i-1}^{\alpha} \hat{\boldsymbol{u}}_i^{\alpha} \right) \left(\frac{\hat{\boldsymbol{u}}_{i-1}}{b_{i-1}} \right) \right], \qquad i = 1 \tag{1.68b}$$

$$\boldsymbol{F}_i^{\mathrm{B}} = \frac{B}{a} \left[\frac{\hat{\boldsymbol{u}}_{i-2} + \hat{\boldsymbol{u}}_i}{b_{i-1}} - \frac{\hat{\boldsymbol{u}}_{i-1}}{b_i} + \left(\hat{\boldsymbol{u}}_i^{\alpha} \hat{\boldsymbol{u}}_{i-1}^{\alpha} \right) \left(\frac{\hat{\boldsymbol{u}}_i}{b_i} \right) - \left(\hat{\boldsymbol{u}}_{i-1}^{\alpha} \hat{\boldsymbol{u}}_{i-2}^{\alpha} + \hat{\boldsymbol{u}}_{i-1}^{\alpha} \hat{\boldsymbol{u}}_i^{\alpha} \right) \left(\frac{\hat{\boldsymbol{u}}_{i-1}}{b_{i-1}} \right) \right], \qquad i = N-2 \tag{1.68c}$$

$$\boldsymbol{F}_i^{\mathrm{B}} = \frac{B}{a} \left[\left(\hat{\boldsymbol{u}}_{i-1}^{\alpha} \hat{\boldsymbol{u}}_{i-2}^{\alpha} \right) \left(\frac{\hat{\boldsymbol{u}}_{i-1}}{b_{i-1}} \right) \right], \qquad i = N-1 \tag{1.68d}$$

Here

$$b_i = |\boldsymbol{R}_{i-1} - \boldsymbol{R}_i| \tag{1.69}$$

Stretching force:

$$\boldsymbol{F}_i^{\mathrm{S}} = \frac{H}{a} \left[\hat{\boldsymbol{u}}_i \left(b_i - a \right) - \hat{\boldsymbol{u}}_{i-1} (b_{i-1} - a) \right], \qquad i \neq 0, N-1 \tag{1.70a}$$

$$\boldsymbol{F}_i^{\mathrm{S}} = \frac{H}{a} \left[\hat{\boldsymbol{u}}_i (b_i - a) \right], \qquad i = 0 \tag{1.70b}$$

$$\boldsymbol{F}_i^{\mathrm{S}} = -\frac{H}{a} \left[\hat{\boldsymbol{u}}_{i-1} (b_{i-1} - a) \right], \qquad i = N-1 \tag{1.70c}$$

1.4 Problem Description

We consider a neutrally buoyant elastic filament (see figure 1.5(A)) – inextensible with a bending rigidity B – subject to a bulk shear flow ,

$$\boldsymbol{v}_{\infty} = \dot{\gamma}(L - Y)\hat{\mathrm{x}}, \tag{1.71}$$

where $\hat{\mathrm{x}}$ is the unit vector along the flow direction and Y is the spatial coordinate along the direction of the gradient of velocity. We denote x, y, z as the coordinate axes, and X, Y, Z as the position. The strain-rate $\dot{\gamma}$ is time-periodic with a period T, $\dot{\gamma} = S\sin(\omega t)$, where $\omega = 2\pi/T$ (see figure 1.5 B). The flow parameters, S, T, and dynamic viscosity of the fluid, η, are chosen such that the Re and Re/St is very small.

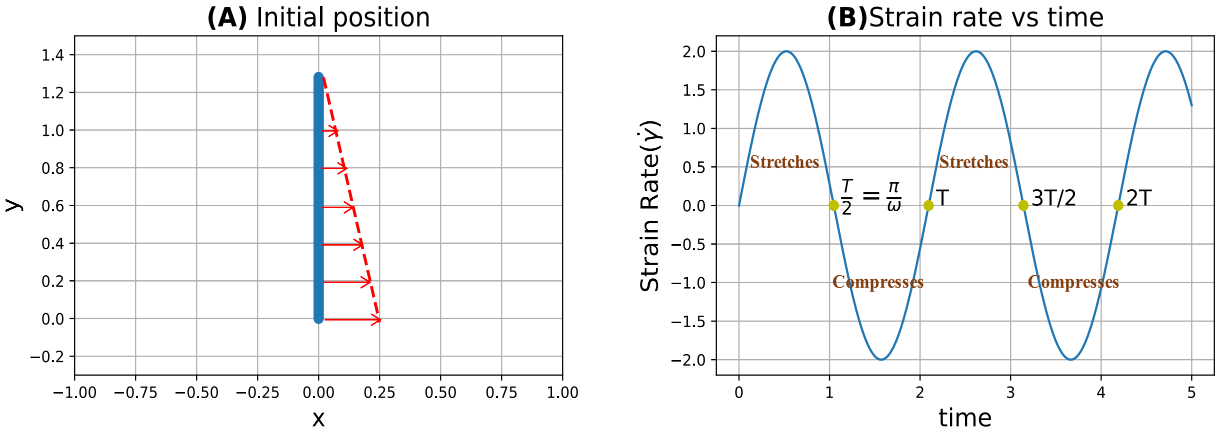

Figure 1.5: Schematic: (A)Filament is freely suspended in the xy plane. Linear shear flow acts along x direction, shown by red arrows. (B) Flow strain rate changes as a Sine function with time.

Our motivation to study the dynamics of a filament in periodically driven Stokes flow comes from the lectures of G.I.Taylor on low-reynolds number flows[2] [40]. In the lecture, he starts with the Taylor-Couette apparatus with a highly viscous fluid. He describes the reversibility of the Stokes flow by putting some dye in syrup in the Taylor-Couette apparatus (figure 1.6). He rotates the apparatus clockwise with some angle and anti-clock wise with the same angle. Not surprisingly, the dye comes back to its initial position due to the time-reversibility of the flow. The same experiment is repeated for a rigid ring – the ring also comes back to its original orientation. Though if a flexible filament is put in the syrup, the filament breaks the kinematic reversibility and does not come back to its original shape but in a buckled state. In this study, we explore this buckling due to the viscous force in details.

We consider a plane-Couette flow without boundaries instead of a circular one. Initially the filament is oriented along the y direction (see figure 1.5A). If the bending rigidity of the

---

[2] Video to the lecture: https://youtu.be/51-6QCJTAjU

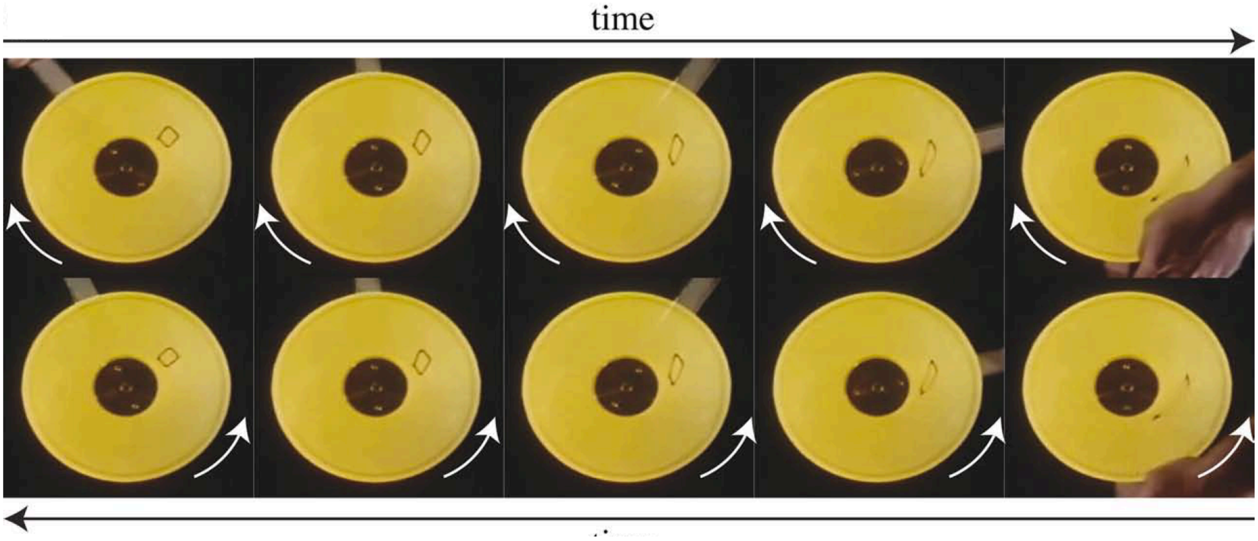

Figure 1.6: Kinematic reversibility of Stokes flow demonstrated by G.I.Taylor. He puts dye in syrup in the apparatus and rotates it with some angle in clockwise direction and in anticlockwise direction with the same angle. The dye comes back to its original position.

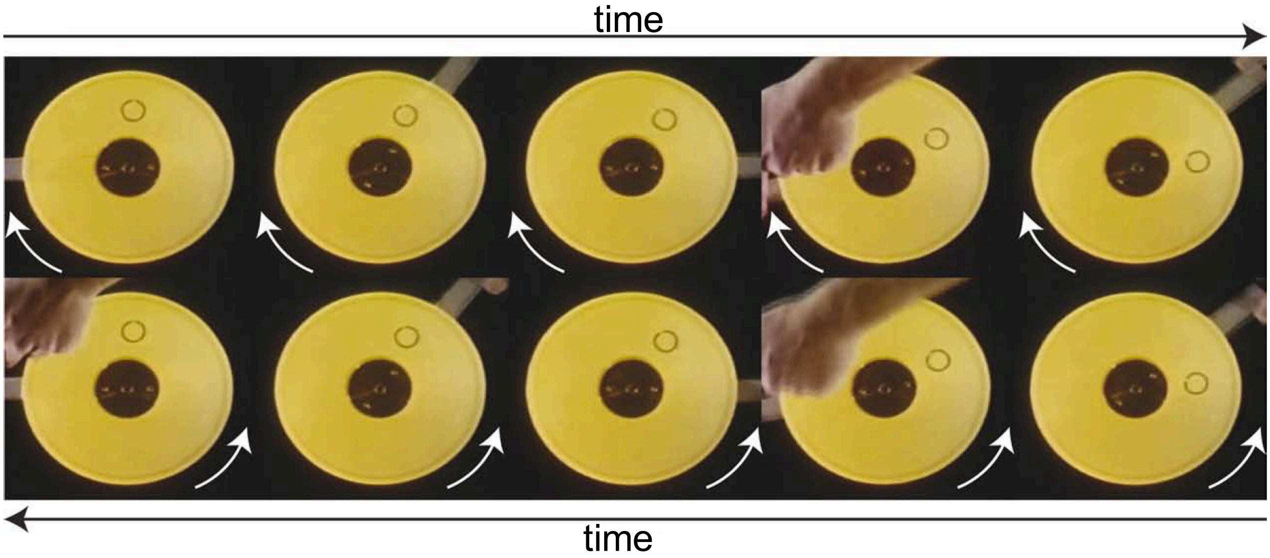

Figure 1.7: G.I.Taylor puts a rigid ring in the apparatus. The ring comes back to its original position with the same orientation after reversing the flow. The little hole in the ring gives information about the orientation of the ring.

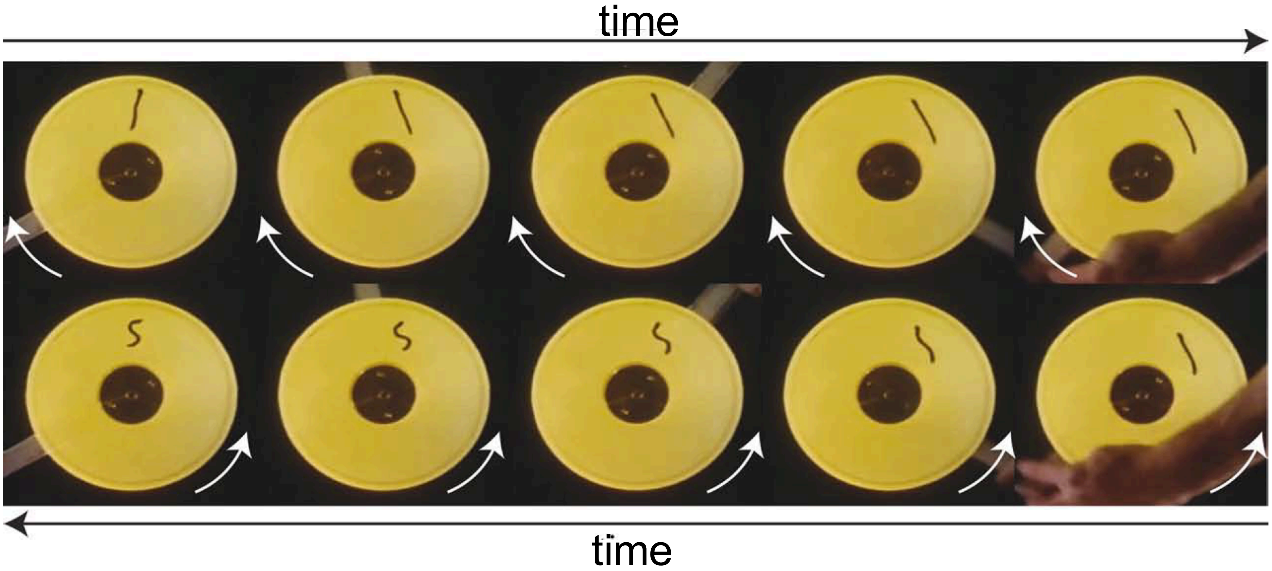

Figure 1.8: G.I.Taylor puts a flexible but inextensible filament in the apparatus. The filament breaks kinematic reversibility and does not come back to its original shape but comes back in the buckled shape after reversing the flow.

filament is very large, such that the filament behaves effectively like a rigid body, we expect the filament to rotate away and back to its original position and shape (similar to the rigid ring in Stokes flow as shown in figure 1.7). An elastic filament of length L, in a time-invariant flow can buckle into different morphologies [41, 42, 43, 44, 45, 32, 46, 47] or even curl up into helical shapes [48] depending on its elastoviscous number $\overline{\mu} = (8\pi\eta S L^4)/B$. Hence, once the bending rigidity is below a threshold, we expect the filament to buckle (similar to figure 1.8) – it would not return to its original shape. The time reversibility would be broken. If the bending rigidity is decreased further we expect elastic nonlinearities to play a more and more dominant role in the dynamics thereby giving rise to higher order bucklings. Repeating the experiments over many cycles can potentially give rise to complex spatiotemporal behaviour of the filament. In this thesis, we investigate the fate of the filament and the flow around it for a large range of bending rigidity and time-period.

References

1. Goldstein, R. E. Green algae as model organisms for biological fluid dynamics. *Annual review of fluid mechanics* **47,** 343–375 (2015).
2. Sebastian, B. & Dittrich, P. S. Microfluidics to mimic blood flow in health and disease. *Annual review of fluid mechanics* **50,** 483–504 (2018).
3. Lighthill, J. Flagellar hydrodynamics. *SIAM review* **18,** 161–230 (1976).

4. Fauci, L. J. & Dillon, R. Biofluidmechanics of reproduction. *Annu. Rev. Fluid Mech.* **38,** 371–394 (2006).
5. Di Carlo, D. Inertial microfluidics. *Lab on a Chip* **9,** 3038–3046 (2009).
6. Squires, T. M. & Quake, S. R. Microfluidics: Fluid physics at the nanoliter scale. *Reviews of modern physics* **77,** 977 (2005).
7. Aref, H. *et al.* Frontiers of chaotic advection. *Reviews of Modern Physics* **89,** 025007 (2017).
8. Taylor, G. I. & Friedman, J. Low Reynolds number flows (1985).
9. Landau, L. & Lifshitz, E. Theory of Elasticity,(Pergamon Press, Oxford, 1986).
10. Audoly, B. & Pomeau, Y. in *Peyresq Lectures On Nonlinear Phenomena* 1–35 (World Scientific, 2000).
11. Fedosov, D. A., Noguchi, H. & Gompper, G. Multiscale modeling of blood flow: from single cells to blood rheology. *Biomechanics and modeling in mechanobiology* **13,** 239–258 (2014).
12. Shelley, M. J. The dynamics of microtubule/motor-protein assemblies in biology and physics. *Annual review of fluid mechanics* **48,** 487–506 (2016).
13. Smith, D., Gaffney, E. & Blake, J. Modelling mucociliary clearance. *Respiratory physiology & neurobiology* **163,** 178–188 (2008).
14. Harasim, M., Wunderlich, B., Peleg, O., Kröger, M. & Bausch, A. R. Direct observation of the dynamics of semiflexible polymers in shear flow. *Physical review letters* **110,** 108302 (2013).
15. Acheson, D. *Elementary fluid dynamics: Oxford University Press* 1990.
16. Batchelor, C. K. & Batchelor, G. *An introduction to fluid dynamics* (Cambridge university press, 2000).
17. Feynman, R. P. *The Feynman Lectures on Physics Vol 2* (Narosa, 1986).
18. Childress, S. *Mechanics of swimming and flying* (Cambridge University Press, 1981).
19. Kim, S. & Karrila, S. J. *Microhydrodynamics: principles and selected applications* (Courier Corporation, 2013).
20. Guazzelli, E. & Morris, J. F. *A physical introduction to suspension dynamics* (Cambridge University Press, 2011).
21. Faxén, H. Der Widerstand gegen die Bewegung einer starren Kugel in einer zähen Flüssigkeit, die zwischen zwei parallelen ebenen Wänden eingeschlossen ist. *Annalen der Physik* **373,** 89–119 (1922).
22. Batchelor, G. & Green, J.-T. The hydrodynamic interaction of two small freely-moving spheres in a linear flow field. *Journal of Fluid Mechanics* **56,** 375–400 (1972).
23. Brady, J. F. & Bossis, G. Stokesian dynamics. *Annual review of fluid mechanics* **20,** 111–157 (1988).

24. Pozrikidis, C. MICROHYDRODYNAMICS: PRINCIPLES AND SELECTED APPLICATIONS by Sangtae Kim, Seppo J. Karilla. *Chemical Engineering Education* **28,** 166–167 (1994).
25. Schwörer, D. *Rotne–Prager based hydrodynamics on GPUs* PhD thesis (Max Planck Institute for Intelligent Systems, 2015).
26. Wada, H. & Netz, R. R. Non-equilibrium hydrodynamics of a rotating filament. *EPL (Europhysics Letters)* **75,** 645 (2006).
27. Powers, T. R. Dynamics of filaments and membranes in a viscous fluid. *Reviews of Modern Physics* **82,** 1607 (2010).
28. Crenshaw, H. C. & Edelstein-Keshet, L. Orientation by helical motion—II. Changing the direction of the axis of motion. *Bulletin of mathematical biology* **55,** 213–230 (1993).
29. Antman, S. S. in *Nonlinear Problems of Elasticity* 603–628 (Springer, 1995).
30. Chaikin, P & Lubensky, T. *Introduction to Condensed Matter Physics* 1995.
31. Goldestein, H. *Classical mechanics, Massachusetts* 1980.
32. Żuk, P. J., Słowicka, A. M., Ekiel-Jeżewska, M. L. & Stone, H. A. Universal features of the shape of elastic fibres in shear flow. *Journal of Fluid Mechanics* **914** (2021).
33. Montesi, A., Morse, D. C. & Pasquali, M. Brownian dynamics algorithm for bead-rod semiflexible chain with anisotropic friction. *The Journal of chemical physics* **122,** 084903 (2005).
34. Bergou, M., Audoly, B., Vouga, E., Wardetzky, M. & Grinspun, E. Discrete viscous threads. *ACM Transactions on Graphics (TOG)* **29,** 1–10 (2010).
35. Wada, H. & Netz, R. R. Stretching helical nano-springs at finite temperature. *EPL (Europhysics Letters)* **77,** 68001 (2007).
36. Bergou, M., Wardetzky, M., Robinson, S., Audoly, B. & Grinspun, E. in *ACM SIGGRAPH 2008 papers* 1–12 (2008).
37. Press, W. H., Teukolsky, S. A., Vetterling, W. T. & Flannery, B. P. *Numerical recipes 3rd edition: The art of scientific computing* (Cambridge university press, 2007).
38. Press, W. H. & Teukolsky, S. A. Adaptive Stepsize Runge-Kutta Integration. *Computers in Physics* **6,** 188–191 (1992).
39. Cash, J. R. & Karp, A. H. A variable order Runge-Kutta method for initial value problems with rapidly varying right-hand sides. *ACM Transactions on Mathematical Software (TOMS)* **16,** 201–222 (1990).
40. Taylor, G. I. Film notes for low-Reynolds-number flows. *National Committee for Fluid Mechanics Films* **21617** (1967).
41. Becker, L. E. & Shelley, M. J. Instability of elastic filaments in shear flow yields first-normal-stress differences. *Physical Review Letters* **87,** 198301 (2001).
42. Guglielmini, L., Kushwaha, A., Shaqfeh, E. S. & Stone, H. A. Buckling transitions of an elastic filament in a viscous stagnation point flow. *Physics of Fluids* **24,** 123601 (2012).

43. Liu, Y., Chakrabarti, B., Saintillan, D., Lindner, A. & Du Roure, O. Morphological transitions of elastic filaments in shear flow. *Proceedings of the National Academy of Sciences* **115,** 9438–9443 (2018).
44. LaGrone, J., Cortez, R., Yan, W. & Fauci, L. Complex dynamics of long, flexible fibers in shear. *Journal of Non-Newtonian Fluid Mechanics* **269,** 73–81 (2019).
45. Slowicka, A., Stone, H. A. & Ekiel-Jezewska, M. L. Flexible fibers in shear flow: attracting periodic solutions. *arXiv preprint arXiv:1905.12985* (2019).
46. Kuei, S., Słowicka, A. M., Ekiel-Jeżewska, M. L., Wajnryb, E. & Stone, H. A. Dynamics and topology of a flexible chain: knots in steady shear flow. *New Journal of Physics* **17,** 053009 (2015).
47. Hu, S.-Y., Chu, J.-J., Shelley, M. J. & Zhang, J. Lévy Walks and Path Chaos in the Dispersal of Elongated Structures Moving across Cellular Vortical Flows. *Physical Review Letters* **127,** 074503 (2021).
48. Chakrabarti, B. *et al.* Flexible filaments buckle into helicoidal shapes in strong compressional flows. *Nature Physics,* 1–6 (2020).

Chapter 2

Results

> Not only in research but also in the everyday world of politics and economics, we would all be better off if more people realized that simple nonlinear systems do not necessarily possess simple dynamical properties.
>
> – Robert May, 1976

2.1 Dimensionless parameters

We define three dimensionless parameters. First, the elasto-viscous number,

$$\overline{\mu} = \frac{8\pi\eta S L^4}{B}, \tag{2.1}$$

second, non-dimensional frequency,

$$\sigma = \frac{\omega}{S}, \tag{2.2}$$

and third, stretching-bending modulus ratio,

$$K = \frac{Hd^2}{B}. \tag{2.3}$$

Where S is amplitude of strain rate, L is length of the filament. The elasto-viscous number $\overline{\mu}$, characterizes the competition between elastic and viscous forces, σ is the ratio of time-scales of external strain rate and rate of change of strain, and K determines the extensibility of filament during simulation. All the parameter values are shown in in table 2.1. The σ must be small enough such that the Stokesian approximation remains valid. We use $K = 16$ (see table 2.1) for all the simulations. The total length of the filament changes at most by 2% – the filament is practically inextensible [1].

2.2 Dynamical phases

Our simulations reveal five different dynamical phases which we call – straight, buckling, two-period, complex and complex transients (see figure 2.1). For each case, we concentrate on two aspects. First, we describe the dynamics through the morphology of the filament. This we do in two ways:

Parameters	**Simulation values**
Number of beads, N	256
Equilibrium distance between beads, a	0.005
Filament diameter, d	0.005
Filament length, L	1.28
Bending modulus, B	2×10^{-5}–8×10^{-3}
Strain Rate amplitude, S	2
Viscosity, η	10
Rate of change of strain rate, ω	1–6
Time-step, Δ	10^{-4}–10^{-6}
Elasto-viscous number, $\overline{\mu} = \frac{8\pi\eta S L^4}{B}$	1.7×10^5–6.8×10^7
Frequency parameter, $\sigma = \frac{\omega}{S}$	0.5–3
Stretching-bending modulus ratio, $K = \frac{Ha^2}{B}$	16

Table 2.1: Parameters of simulation. Earlier studies have used $N = 20 - 40$ [1], $N = 40$ [2], N=400 [3]

(a) Extrinsic (real space) – actual shape of the filament.

(b) Intrinsic (configurational space) – curvature (κ) of the filament as a function of arc-length (s). Our definition of dynamical phase is based on this analysis of the filament. Conversion from extrinsic to intrinsic coordinate is done using equation 1.63a – this conversion is unique. Although the inverse is not true. However, if we fix the position of the first bead and slope of the bond to the next one, intrinsic to extrinsic coordinate transformation is unique.

Second, we look at the velocities at Eulerian and Lagrangian points in the flow.

2.2.1 Straight (S)

We see that the filament does not develop any buckling instability and returns to its original shape i.e. straight configuration for after every cycle. Intrinsically, the curvature remains zero everywhere.

2.2.2 Periodic buckling (B)

The filament develops buckling instability. The filament settles into periodic behavior after an initial transients and repeats itself stroboscopically (after every cycle) both extrinsically and intrinsically [see figure 2.2 (A)].

2.2.3 Two-period (2P)

Intrinsically, the filament does not repeat itself after every period but after every two periods (see figure 2.2(B)). Extrinsically, the filament does not come back to its position but in rotated position after two-cycles – which we call swimming [see figure 2.3].

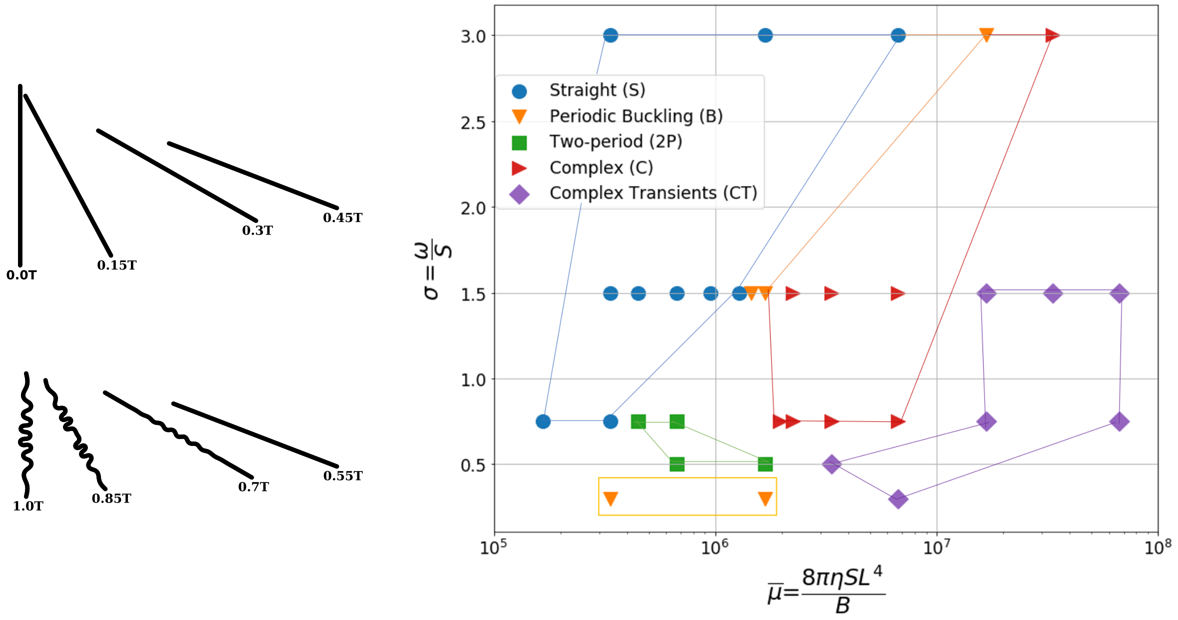

Figure 2.1: (Left) Evolution of a straight filament freely suspended in shear flow $\boldsymbol{U} = \dot{\gamma}(L - Y)\hat{\mathrm{x}}$ with $\dot{\gamma} = S\sin(\omega t)$ over one period $T = 2\pi/\omega$ from our simulations. During the first-half of the period, $t = 0$ to $T/2$ the filament translates and rotates. During the second half it translates and rotates back but in addition buckles to a complex shape.

(Right) Phase diagram from time-dependent numerical simulations in the $\overline{\mu}$–σ parameter space. The phase-diagram is based on the filament dynamics in the intrinsic coordinate system. $\left(\sigma = \frac{\omega}{S}, \overline{\mu} = \frac{8\pi\eta SL^4}{B}\right)$. Here ω is rate of change of strain, S is strain rate, η is the viscosity, L is length of the filament, and B is the bending modulus. Initially, the filament is freely suspended in the shear flow. We find 5 different dynamical phases in the system represented by 5 symbols. **(S)** Straight:- The filament comes back to the initial position in the straight configuration after every period. **(B)** Periodic buckling:- The filament comes back in the buckled configuration after every period. **(2P)** Two-period :- The filament repeats its configuration not after every but after two-period. **(C)**Complex:- The filament buckles into complex shape with very high mode of buckling instability. **(CT)** Complex transients :- Filament shows long transients with complex shape but at late times, the shape of the filament repeats itself.

2.2.4 Complex (C)

The filament rotates in the first half of the cycle (see figure 2.1 (left)). In the second half, it buckles with high mode. We compare the sine transform for two different phases in figure 2.4. The complex phase shows high mode of buckling instability i.e. peaks at high wavenumbers. In figure 2.5 (A), we plot the filament at the end of 1st, 10th, 19th, 28th and 37th cycle for $\overline{\mu} = 3.35 \times 10^6$, $\sigma = 1.5$) – the filament never repeats itself. In figure 2.5 (B), we plot the curvature (κ) of the filament as a function of arc-length (s) at the same times. This shows too that the shape of the filament never repeats at the end of each cycle. Even at late times $t > 40T$, the filament does not repeat itself at the end of a cycle – see figure 2.5 (C) where we plot the shape of the filament at $t = 35T, 45T, ..., 75T$. The corresponding plot of κ versus s is

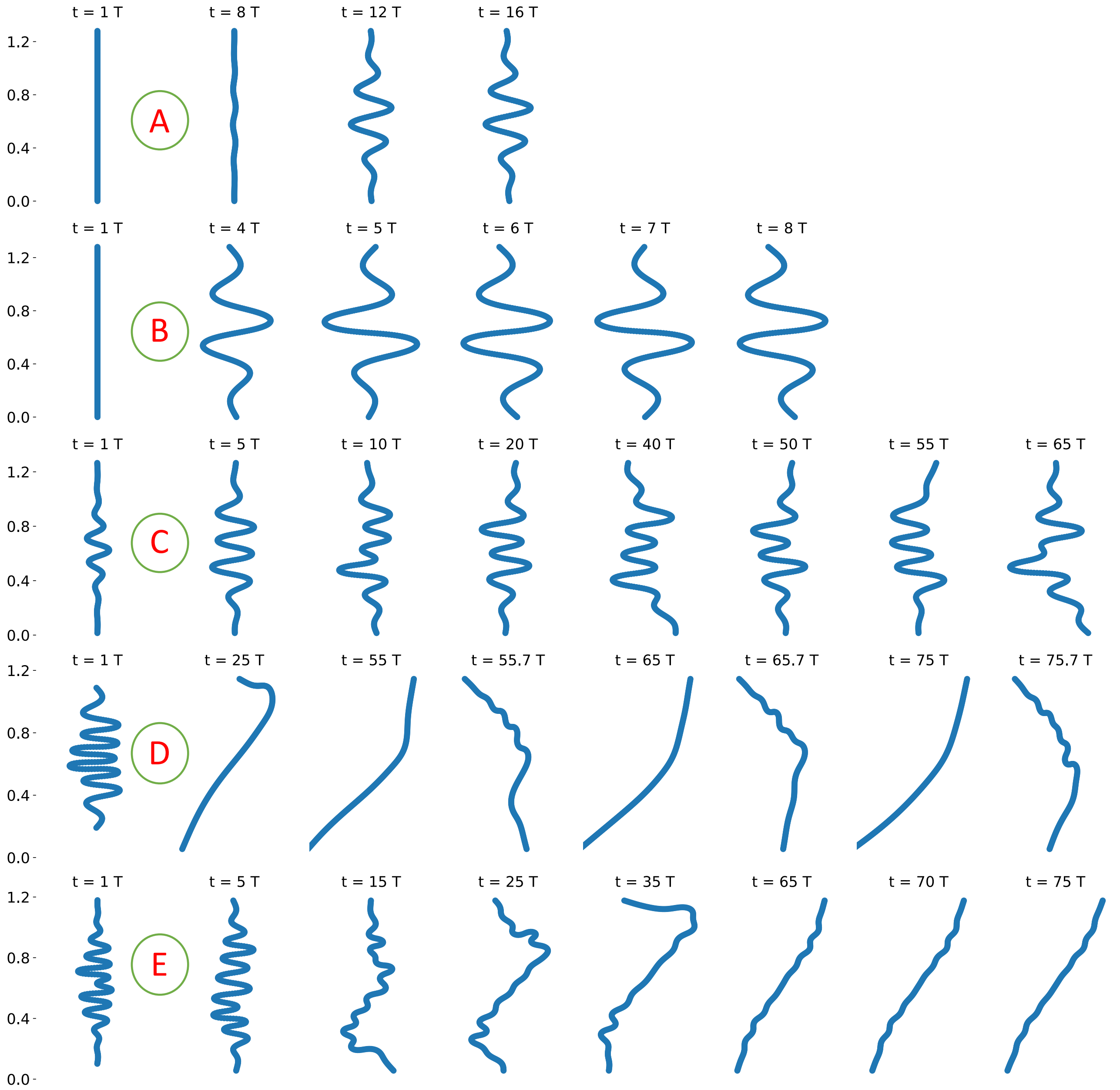

Figure 2.2: Representative snapshots of the filament in real space. (A) Periodic buckling ($\overline{\mu} = 1.46 \times 10^6$, $\sigma = 1.5$): The filament develops buckling instability after 8 cycles and repeats itself after every cycle. Although the filament looks straight from $t = T$–$7T$, it is little deformed from a straight configuration. (B) Two-period ($\overline{\mu} = 0.67 \times 10^6$, $\sigma = 0.75$): The filament repeats its configuration after two-cycles but in real space it comes back rotated from earlier position. (C)Complex ($\overline{\mu} = 3.35 \times 10^6$, $\sigma = 1.5$): The filament always shows spatiotemporally complex behavior and never repeats itself stroboscopically. (D) Complex ($\overline{\mu} = 6.7 \times 10^6$, $\sigma = 0.75$): The filament shows spatiotemporally complex behavior and comes very close to repeating itself at the end of a cycle. Although the filament shows maximum buckling somewhere in the middle of cycle e.g. t=55.7T..75.7T, and we find that the filament does not repeat itself if we compare the shape at t = 55.7T .. 75.7T. (E) Complex transients($\overline{\mu} = 16.75 \times 10^6$, $\sigma = 1.5$): Filament shows spatiotemporally complex behavior but repeats itself everywhere for late cycles.

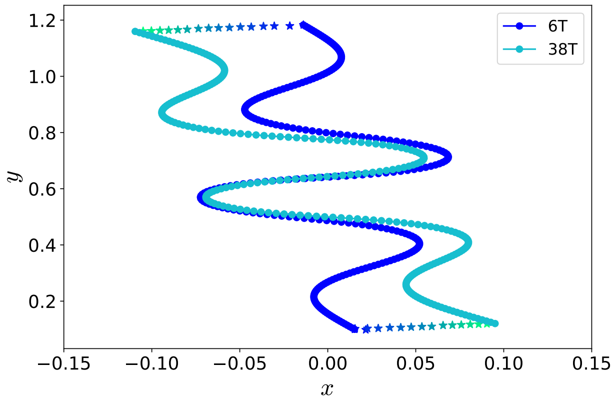

Figure 2.3: Demonstration of swimming for the two-period phase ($\overline{\mu} = 6.7 \times 10^5$, $\sigma = 0.75$). We show the extrinsic plots of the filament for $t = 6T$ and $t = 38T$. Intrinsically, the filament repeats itself after every two-period. However, the filament rotates by some angle in clockwise direction after every two-periods. We show the end of the filament for intermediate times $t = 8T, 10T, \ldots, 38T$ by stars, which shows swimming of the filament.

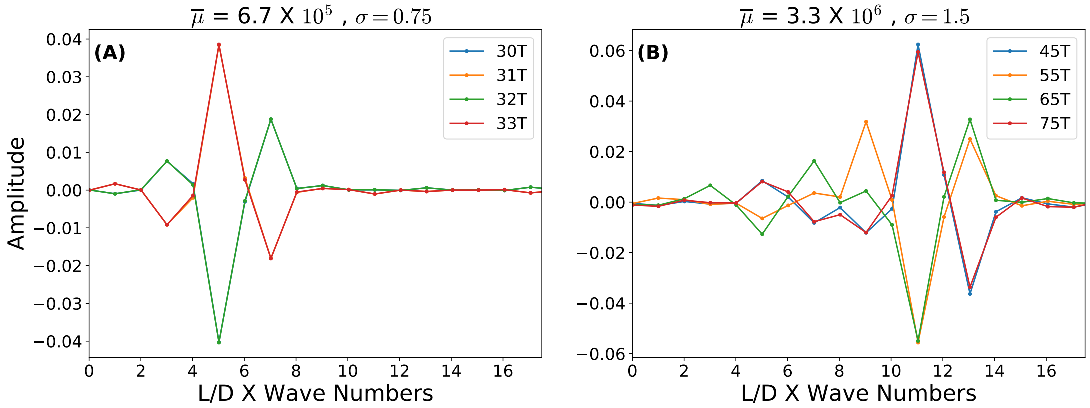

Figure 2.4: Comparison of discrete sine transform for two-period phase (A), and complex phase (B). The filament shows higher modes of buckling instability comparatively in the complex phase. In figure A, green and red colour plots ($t = 32T, 33T$) hide the plots with green and orange colour ($t = 30T, 31T$) as they lie on top of each other.

shown in figure 2.5 (D). Here it may seem that the filament comes close to its previous shapes but a careful look tells us that it never completely repeats itself. Note that, the $\kappa - s$ plot for $t = 35T$ is very close to the one at $t = 65T$, although not exactly the same. The same is true for $t = 45T$ and $t = 75T$. This suggests that there maybe a very high period solution to the stroboscopic map that we discuss in section 2.3.

Note that, in some cases of this complex phase, at late times, the filament achieves the most buckled state (as measured by total elastic energy) not at the end of the cycle but somewhere in middle. One such case is shown in figure 2.6 for $\overline{\mu} = 6.7 \times 10^6$ and $\sigma = 0.75$. The κ–s plot at the end of every cycle comes very close to repeating itself – figure 2.6 (B). The corresponding plots of the filament in real space, is shown in figure 2.6 (A), is also very close to one another although does not overlap everywhere. However, if we look at intermediate times e.g. at $t = 65.7T ... 75.7T$, we find that the filament does not repeat itself – see figure 2.6 (C,D).

To measure the disturbances in the flow due to moving filament, we calculate the time series data of flow disturbance $\boldsymbol{V}(\boldsymbol{X})$ at an Eulerian point $\boldsymbol{X}$ (equation 1.32). We take $\boldsymbol{X} = [0, L/2, 2d]$. The Eulerian point is strategically chosen to be just above the xy plane so that the filament does not overlap with the Eulerian point. We slice the 3-dimensional time series data of $\boldsymbol{V}(\boldsymbol{X})$ to xy and yz plane. We show the phase portraits of $S\boldsymbol{V}/L$ at late times ($t = 40T$ to $t = 75T$) in figure 2.5, 2.6 (E,F) respectively. Note that, the velocity attains higher values as compared to the straight phase (compared in figure 2.5 (E,F)).

We observe different kind of behavior at the phase border between 'B' and 'C' ($\overline{\mu} = 3.3 \times 10^6, \sigma = 1.5$). Overall, the filament does not settle into any periodic behavior for long cycles but shows periodic behavior for shorter cycles. The filament shows periodic behavior for for few cycles, but later the filament moves to different pattern which continues further. The filament has some transient dynamics in between both the patterns.

2.2.5 Complex transients:

The filament shows high mode of buckling. We compare the filament extrinsically and intrinsically at the end of 14th, 24th, 34th, 44th cycle for $\overline{\mu} = 16.75 \times 10^6, \sigma = 1.5$ respectively in figure 2.7 (A)(B). The filament shows complex behavior and does not repeat itself for early periods ($t < 50T$). However the complex behavior is transient and the filament settles into a periodic behavior and comes very close to itself for late periods – at the end of a cycle ($t = 64T, 68T, 74T$, see figure 2.7 (C)) and intermediate times between cycle where the filament shows maximum buckling ($t = 60.8T, 64.8T, 68.8T, 74.8T$, see figure 2.7 (E)). The corresponding plots of $\kappa - s$ is shown in figure 2.7 (D)(F) – this also shows the periodic behavior of filament at late times. Figure 2.7(G,H) shows fluctuations of flow velocity at $\boldsymbol{X} = [0, L/2, 2d]$ for late times ($t > 55T$). We see that the flow also does not show any complex behavior.

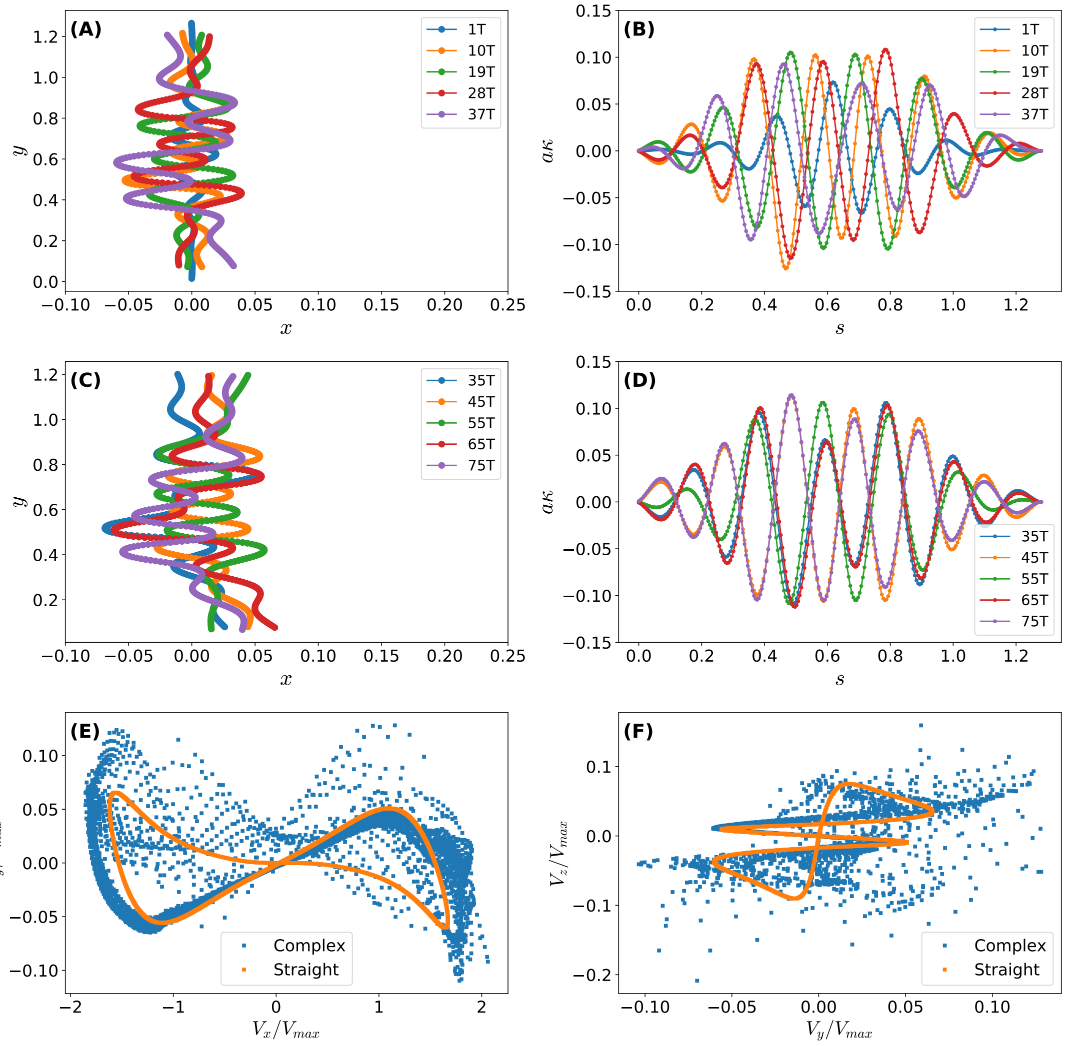

Figure 2.5: Evolution of the filament for complex phase ($\overline{\mu} = 3.35 \times 10^6$, $\sigma = 1.5$). (A,B) The filament shows complex behavior at early cycles ($t = \mathrm{T}, 10\mathrm{T}, 19\mathrm{T}, 28\mathrm{T}, 37\mathrm{T}$) in extrinsic and intrinsic coordinate respectively. (C,D) We plot the filament in extrinsic and intrinsic coordinate for late cycles ($t = 35\mathrm{T}, 45\mathrm{T}, 55\mathrm{T}, 65\mathrm{T}, 75\mathrm{T}$). The filament comes very close to itself after ~ 30 cycles ($t = 35\mathrm{T}\&65\mathrm{T}$, $t = 45\mathrm{T}\&75\mathrm{T}$) but does not repeat itself. (E,F) We show the phase portrait of velocity disturbances at an Eulerian point (see equation 1.32) $\boldsymbol{X} = \left[0, \frac{L}{2}, 2d\right]$ for late cycles $t = 45\mathrm{T} - 75\mathrm{T}$ for complex ($\overline{\mu} = 3.35 \times 10^6$, $\sigma = 1.5$) and straight ($\overline{\mu} = 3.35 \times 10^7$, $\sigma = 1.5$) phase.

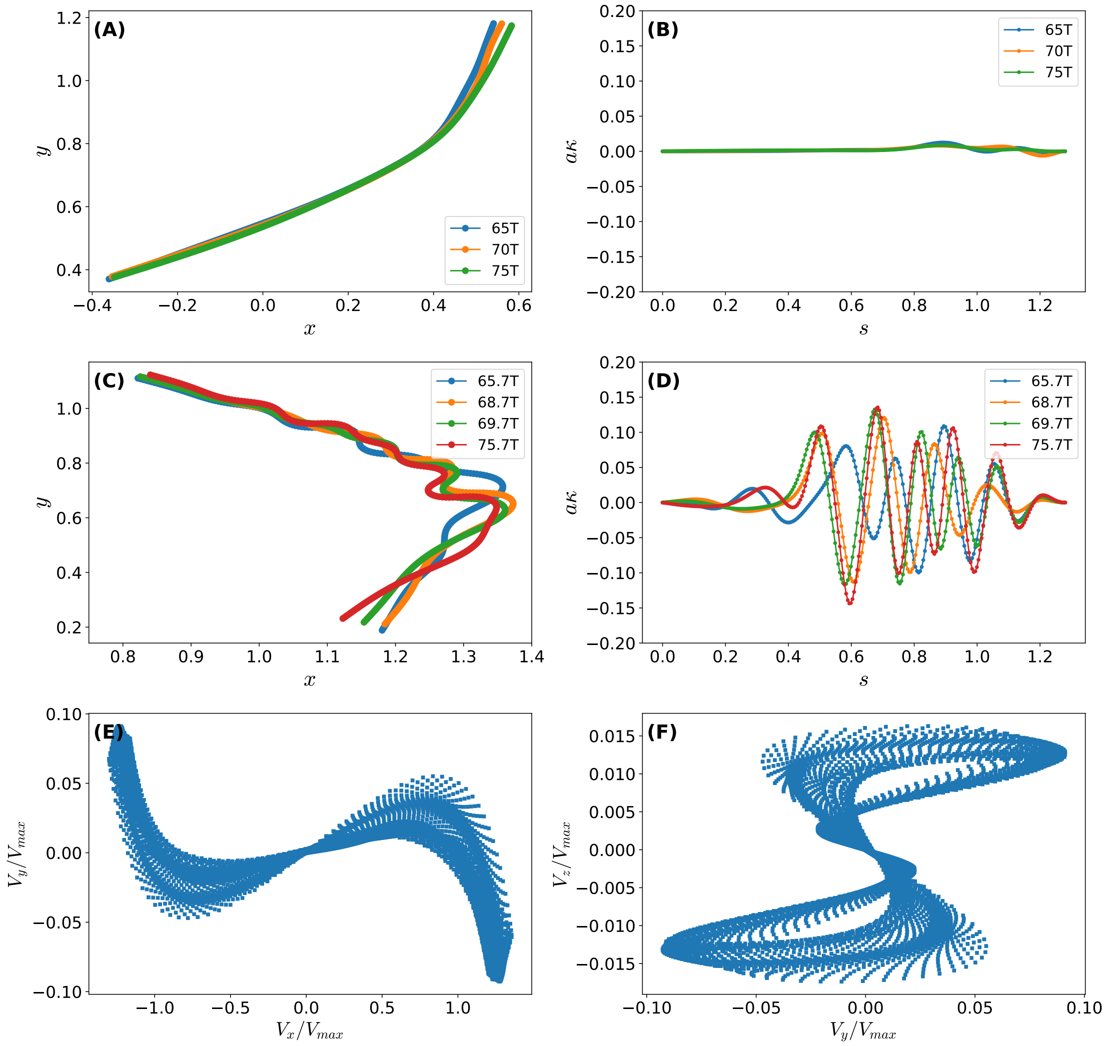

Figure 2.6: Evolution of the filament for $\overline{\mu} = 6.7 \times 10^6$, $\sigma = 0.75$. (A,B) For late times, we compare the filament at nT and see that the filament comes very close to repeating itself.(C,D) We compare the filament where it shows the maximum compression in a cycle (measured by bending energy) – for this point in the phase diagram, we choose to compare the filament at $nT + 0.7T$. We observe that the filament shows complex behavior and does not repeat itself. (E,F) Phase portrait of velocity disturbances at Eulerian point $\boldsymbol{X} = \left[0, \frac{L}{2}, 2d\right]$ in xz and yz plane.

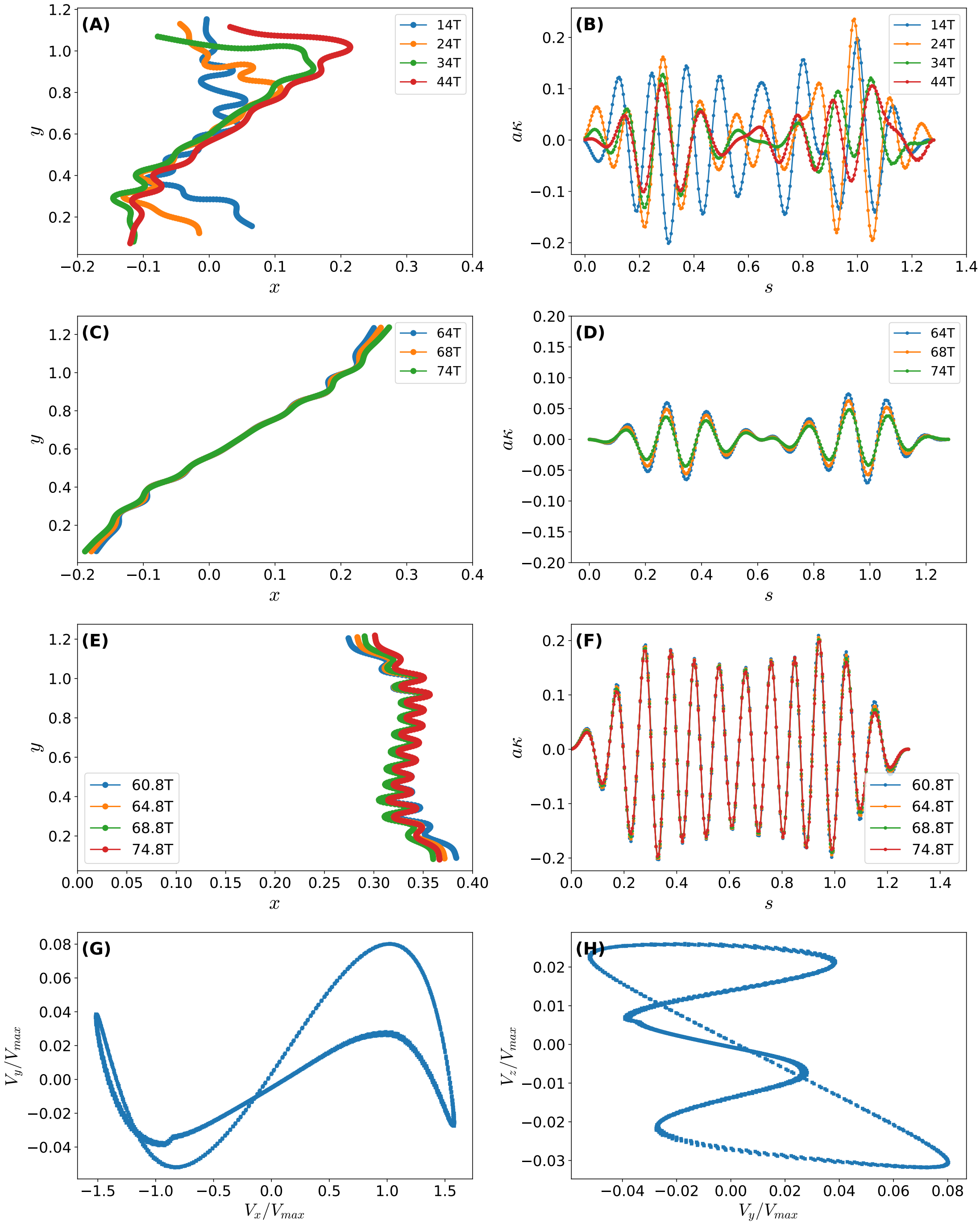

Figure 2.7: Evolution of the filament for the complex transient phase. $\overline{\mu} = 16.75 \times 10^6$, $\sigma = 1.5$. We compare the filament extrinsically(A) and intrinsically (B) for early periods. The filament shows complex behavior and does not repeat itself for early cycles. (C,D) However the filament repeats itself extrinsically(C) and intrinsically(D) at the end of the cycle (E,F) We compare the filament in the middle of a cycle, where the filament shows maximum buckling. The filament shows repetitive behavior for that point as well. (G,H) The phase portrait of velocity $\boldsymbol{V}(\boldsymbol{X} = \left[0, L/2, 2d\right])$ in xz and yz plane respectively. The phase portrait shows that the filament settles into a periodic state for late periods.

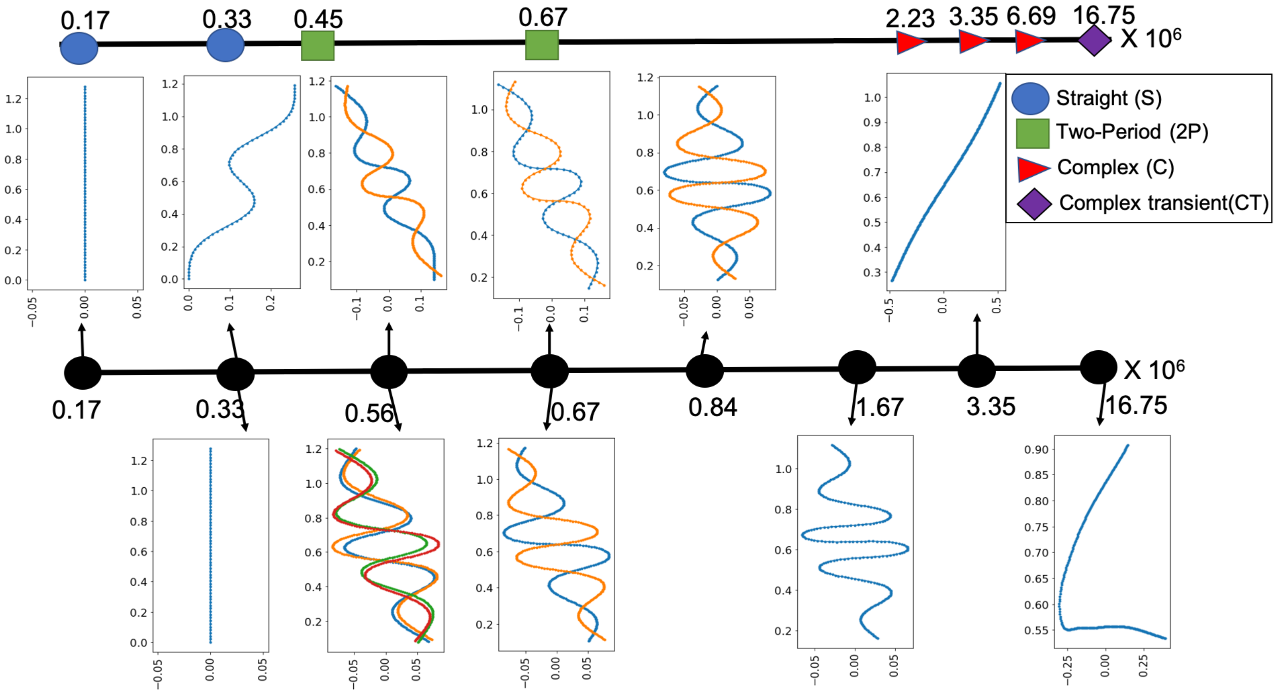

Figure 2.8: We plot the different co-existing solutions of stroboscopic map (equation 2.5) in real space for $\sigma = 0.75$ for different $\overline{\mu}$. Note that, the solutions of the map are in curvature space, we just show the corresponding real space plots of the solutions. We find multiple co-existing solutions as we increase $\overline{\mu}$ (black symbols from left to right) indicating the complexity of the system. We compare the solutions with the phase diagram from evolution code (see figure 2.1(right))

2.3 Stroboscopic map

We take a dynamical system approach to analyze the complex dynamics we observe. Such techniques have been used widely to study highly turbulent flows [4, 5, 6] – first envisioned by Hopf [7] – and has also been applied to other fields of fluid dynamics [8, 9].

Let us define an operator $\mathcal{M}$ such that:

$$\boldsymbol{\kappa}(T) = \mathcal{M}\boldsymbol{\kappa}(0) \tag{2.4a}$$

$$\mathcal{M}^{\mathrm{p}} = \mathcal{M}\mathcal{M}\ldots\text{p times}\ldots\mathcal{M}, \tag{2.4b}$$

where $\boldsymbol{\kappa} = [\kappa_1, \kappa_2 \ldots \kappa_N]$ and κ_{i} is given as equation 1.63a. For a given $\boldsymbol{\kappa}$, the operator, $\mathcal{M}$, returns the values of $\boldsymbol{\kappa}$ after evolving the system for exactly one time-period. We look for equilibrium points and periodic orbits of this by solving $\boldsymbol{\kappa} = \mathcal{M}^{\mathrm{p}}\boldsymbol{\kappa}$ [10]. The task is now to calculate the solutions of set of the non-linear equations:

$$\mathcal{N}_{\mathrm{p}}\boldsymbol{\kappa} \equiv (\mathcal{M}^{\mathrm{p}} - 1)\,\boldsymbol{\kappa} = 0 \tag{2.5}$$

For example, $\boldsymbol{\kappa} = \mathbf{0}$, $\mathrm{p} = 1$, is a solution for straight phase. The periodic buckling and two-period have non-zero curvature ($\boldsymbol{\kappa}$) solution respectively for $\mathrm{p} = 1$ and $\mathrm{p} = 2$. We use Newton-Krylov method [11] based on Generalized minimal residual method [12] in Jacobian-free way to find the solutions. It is described next.

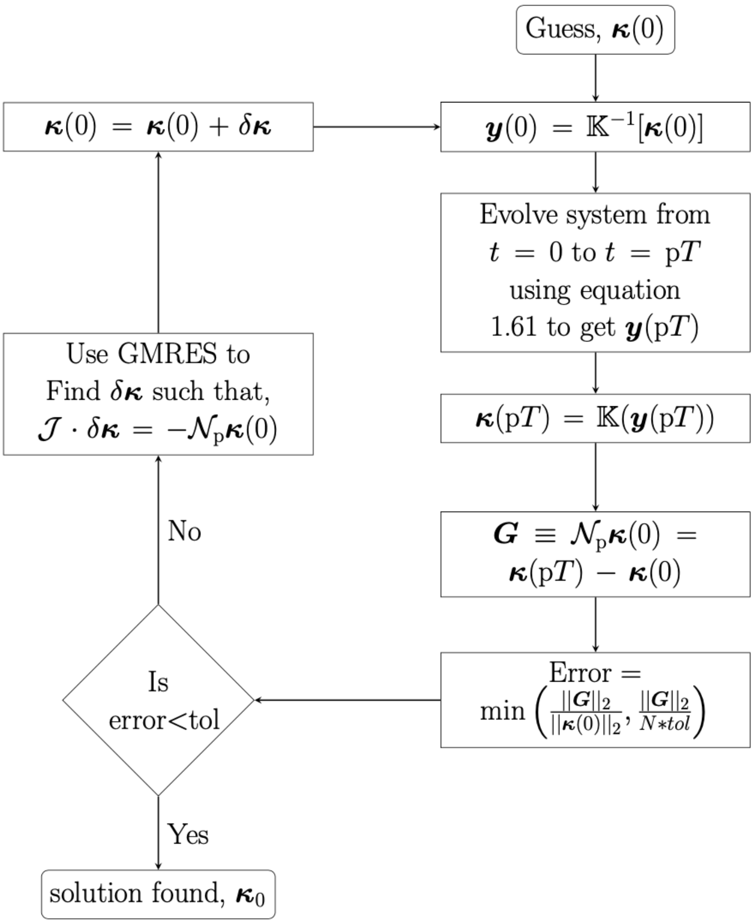

Figure 2.9: Flowchart for Newton-Krylov iteration. $\mathbb{K}$ is co-ordinate transformation from real to curvature space using equation 1.63a.Similarly, $\mathbb{K}^{-1}$ is the inverse coordinate transformation from curvature to real space. We use notation: . $\mathcal{J}$ is jacobian of the operator $\mathcal{N}$, described in equation 2.11. We use $\mathrm{tol} = 0.01$

2.3.1 Newton-Krylov

The flow-chart of the algorithm is shown in figure 2.9. We start with a guess for the curvature, $\boldsymbol{\kappa}(0)$. Then we calculate the positions of the beads given by $\boldsymbol{y} \equiv [R^1_1, R^1_1, \ldots, R^1_j, R^2_j, \ldots, R^1_N, R^2_N]$. We call this transformation $\boldsymbol{\kappa}$ to $\boldsymbol{y}$, $\mathbb{K}^{-1}$, such that:

$$\boldsymbol{y}(0) = \mathbb{K}^{-1}\boldsymbol{\kappa}(0) \tag{2.6}$$

Then we evolve in time from $t = 0$ to $t = \mathrm{p}T$ as described in section 1.3.3 to obtain $\boldsymbol{y}(\mathrm{p}T)$. Then we apply the inverse transformation, $\mathbb{K}$, to obtain

$$\boldsymbol{\kappa}(\mathrm{p}T) = \mathbb{K}(\boldsymbol{y}(\mathrm{p}T)) \tag{2.7}$$

Then we check how accurately equation 2.5 is satisfied, i.e. we define

$$\mathrm{error} = \frac{||\mathcal{N}_{\mathrm{p}}\boldsymbol{\kappa}||_2}{||\boldsymbol{\kappa}(0)||_2}. \tag{2.8}$$

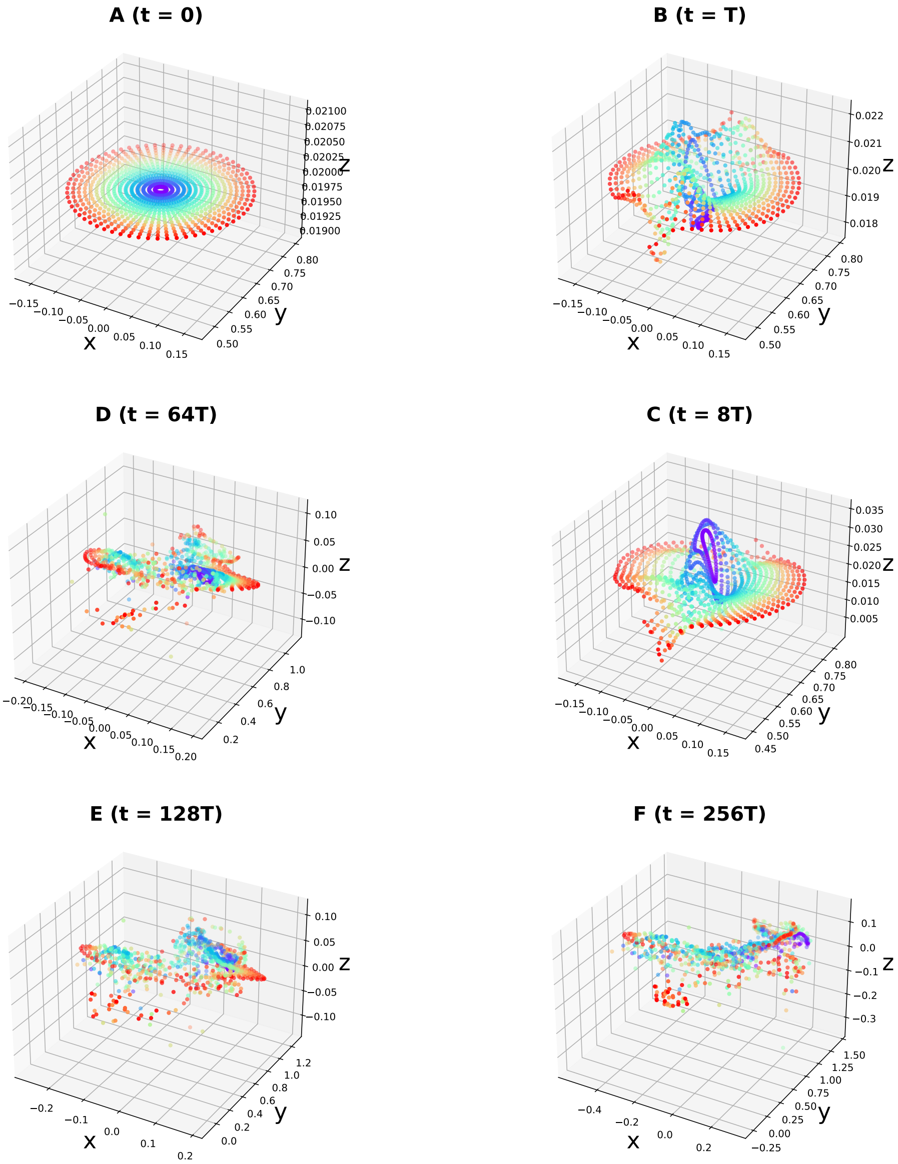

Figure 2.10: Positions of tracer particles stroboscopically in the fluid for complex phase ($\overline{\mu} = 3.3 \times 10^6, \sigma = 1.5$). **(A-F):** We start with concentric circles at $t = 0$. The sheet of tracers starts stretching in y and z direction ($t = T$,$t = 8T$). At later times, we see that the colors are mixed up in the entire region ($t = 64T, 128T, 256T$).

The case for straight solution is dealt specially because in this case $\boldsymbol{\kappa} = 0$. Here we use:

$$\text{error} = \frac{||\mathcal{N}_{\text{p}}\boldsymbol{\kappa}||_2}{N * \text{tol}} \tag{2.9}$$

If the error is less than a preset tolerance, then we accept the guess ($\boldsymbol{\kappa}(0)$) as solution otherwise, we generate a new guess by

$$\boldsymbol{\kappa}(0) = \boldsymbol{\kappa}(0) + \delta\boldsymbol{\kappa}, \tag{2.10a}$$

such that

$$\mathcal{J} \cdot \delta\boldsymbol{\kappa} = -\mathcal{N}\boldsymbol{\kappa}(0). \tag{2.10b}$$

Here $\mathcal{J}$ is Jacobian matrix of the operator $\mathcal{N}_{\text{p}}$ computed at $\boldsymbol{\kappa}(0)$. We calculate:

$$\mathcal{J} \cdot \delta\boldsymbol{\kappa} = \frac{\mathcal{N}_{\text{p}}(\boldsymbol{\kappa}(0) + \epsilon\delta\boldsymbol{\kappa}) - \mathcal{N}_{\text{p}}(\boldsymbol{\kappa}(0) - \epsilon\delta\boldsymbol{\kappa})}{2\epsilon}. \tag{2.11}$$

Here ϵ is a step size [11]. We use the GMRES [12, 13] method in matrix-free way using equation 2.11 to find solutions of 2.10b. The operator $\mathcal{N}_{\text{p}}$ is implemented as described in figure 2.9. The value of ϵ should be small enough such that equation 2.11 is well approximated and large enough so that the floating point round-off errors are not too large [11]. We compute ϵ in the following way:

$$\epsilon = \epsilon_{\text{rel}} \left(1 + \frac{||\boldsymbol{\kappa}(0)||_2}{||\delta\boldsymbol{\kappa}(0)||_2}\right), \tag{2.12}$$

where $|| \cdot ||$ is the 2nd norm, and $\epsilon_{\text{rel}} = 10^{-4}$.

Note that, the conversion from curvature space to real space ($\mathbb{K}^{-1}$) is not unique. However, if we fix the position of the first bead and slope of the bond to the next one, it is unique. One advantage of using this method is that, it accounts for all the continuous symmetries (translation in x,y direction) present in the system [10].

Also note that the $\boldsymbol{\kappa}$ is the same for two filaments which has the same shape but are rotated with respect to each other. But the evolution of two such filaments are not the same, in principle, because the ambient flow depends on space. In some cases, we find the solutions such that the filament comes to the same shape as before but rotated. We call these solutions "swimming solutions" (figure 2.3).

2.3.2 Solutions of the map

We explore the solutions of equation 2.5 for $\sigma = 0.75$. The motive behind this analysis is to show that the system has multiple fixed points and periodic orbits. We find the solutions of the system mainly in two ways. First, we evolve the system from some initial condition (not necessarily straight) till it settles into a periodic orbit (with error $<$ tolerance) with period p. Second, we find the solution using Newton-Krylov method, as described in figure 2.9.

From the evolution phase diagram, we expect that the straight filament is a solution for low enough $\overline{\mu}$. Larger than a particular $\overline{\mu}$, we see the apperance of two-period hence we expect a non-zero solution of equation 2.5 for p = 2. As we increase $\overline{\mu}$ further, we expect many solutions to appear.

In figure 2.8, we show the solutions for 8 different value of $\overline{\mu}$. At the lowest $\overline{\mu} = 1.7 \times 10^5$, we see straight filament as the only solution. This point in the evolution phase diagram is characterized as straight phase. Going towards right, at $\overline{\mu} = 3.3 \times 10^5$, in addition to the straight solution, we see buckled state as a solution as well. This value of $\overline{\mu}$, belongs to straight phase (figure 2.1(right)) in the evolution phase diagram. It is possible in two ways. 1) The straight filament is not a stable solution for $\overline{\mu} = 3.3 \times 10^5$, so for late times in the evolution, the filament moves away from the straight solution and settles into the buckled state. 2) The straight filament and buckled state both are stable solutions but the filament chooses either of the two depending on the initial condition.

More towards right in the phase diagarm, at $\overline{\mu} = 5.6 \times 10^5$, the filament shows two different solutions of equation 2.5 with $p = 2$, $p = 4$ i.e. two-period and four-period. Further right, at $\overline{\mu} = 6.7 \times 10^5$, the filament shows two different two-period ($p = 2$) solutions – this part of the phase diagram is characterized as two-period phase (figure 2.1(right)). Further right, the solution with four-period disappear at $\overline{\mu} = 8.4 \times 10^5$ and the system shows only one solution for $p = 2$.

We explore the solutions of equation 2.5 in the complex regime. One of the solutions at $\overline{\mu} = 1.67 \times 10^6$, is a buckled state for p = 1 – κ vs s plot of this solution cross x-axis 7 times. Further right, in the complex regime at $\overline{\mu} = 3.35 \times 10^6$, we find an almost straight tilted filament as a fixed point solution.

In the complex transient phase, at $\overline{\mu} = 1.675 \times 10^7$, the filament settles into a periodic state after ~ 60 cycles. We find this periodic state a fixed point solution of the map.

We do not show the solutions of equation 2.5 for $\sigma = 1.5$, we find many solutions for $\sigma = 1.5$ as well. At the border between ‘B’ and ‘C’ of evolution phase diagram (figure 2.1(right)), for $\overline{\mu} = 3.3 \times 10^6$, we find two buckled state as a fixed point (p = 1) solution. At this point, in the evolution diagram, we see that the filament jumps from one periodic state to another state. We find two fixed point (p = 1) solutions for $\overline{\mu} = 3.35 \times 10^7$ as well. Althought the filament settles to one of the solutions after some complex transients, when evolved from a straight configuration.

2.4 Mixing

Earlier, we looked at the velocity fluctuations at an Eulerian point for complex phase(see figure 2.5(E)). Here, we first present qualitative evidences of mixing of Lagrangian tracers in the flow in figure 2.10. Later, we look at the dynamics quantitatively to conclude that the Lagrangian tracers are mixed through diffusive process.

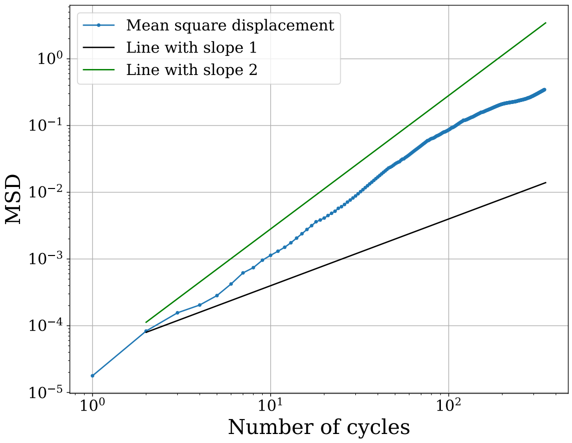

Figure 2.11: Strobosopic average mean square displacement of tracer particles in the fluid for complex phase ($\overline{\mu} = 3.3 \times 10^6, \sigma = 1.5$). We start with concentric circle at $t = 0$ (see figure 2.10(A)).

Dynamics of tracer particles is given as:

$$\dot{X}^{\alpha} = V^{\alpha}(\boldsymbol{X}) + \dot{\gamma}(t)(L - Y)\hat{\mathrm{x}}, \tag{2.13a}$$

$$\dot{\gamma}(t) = S\sin(\omega t) \tag{2.13b}$$

where $\boldsymbol{X} = [X, Y, Z]$, is the position of a tracer particle, $S = 2s^{-1}$. The expression for velocity, V^{α}, is given in equation 1.32. We concentrate on the complex region in the phase diagram with a representative point, $\overline{\mu} = 3.35 \times 10^6, \sigma = 1.5$. We put tracer particles at the end of 10^{th} cycle on concentric circles just above the xy plane, $Z = 0.01$ – we denote this as $t = 0$ in figure 2.10. Every ring is colored based on its distance from the center of the circle. So mixing of colors implies the mixing of the tracers. We show the snapshots of the particles for different times in figure 2.10. At $t = T$, the points on the inner circles have moved out of the xy plane, whereas the outer circles remains almost unchanged, see figure 2.10(B). The picture remains qualitatively the same even at $t = 8T$ although the inner circle come closer to one another and the outer circle gets deformed. At $t = 64T$, we see that the colors of the inner circles are mixed, however the mixing still have not spread to the outer circles. At even later times [figure 2.10(E,F)], the tracer particles look well-mixed. We observe that few tracer particles achieve very high velocities. We suspect, it happens because the particles are crossing the filament – it is not physically possible. Such spurious particles are removed here.

We compute the mean square displacement, $\langle r^2 \rangle$,

$$\boldsymbol{r}^{\mathrm{k}}(p) = \sum_{j=1}^{p-1} \Delta \boldsymbol{X}_j^{\mathrm{k}} \tag{2.14a}$$

$$\langle r^2 \rangle = \frac{1}{M} \sum_{k=0}^{N} \boldsymbol{r}^{\mathrm{k}}(p) \cdot \boldsymbol{r}^{\mathrm{k}}(p), \tag{2.14b}$$

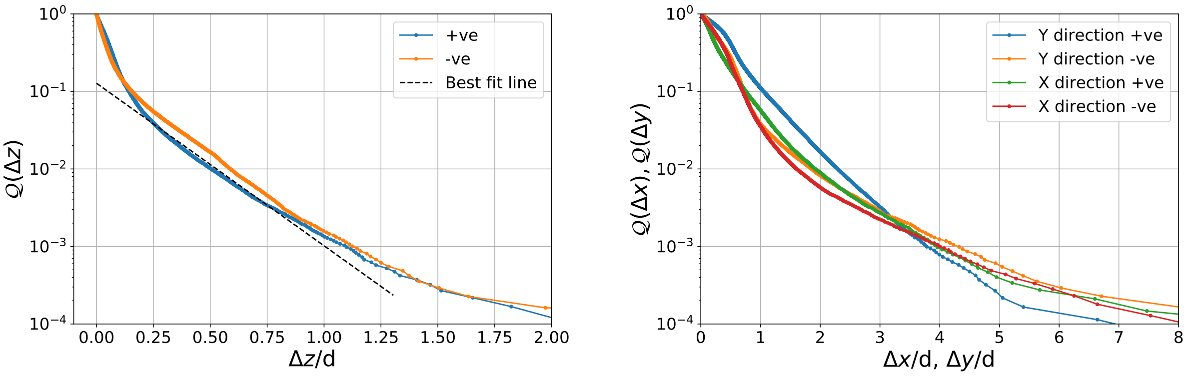

Figure 2.12: Semilog plots of cumulative probability distribution function, $\mathcal{Q}(\xi)$, where $\xi \equiv \Delta x, \Delta y, \Delta z$, (equation 2.15). (Left) ($\xi = \Delta z_+, \Delta z_-$) A straight line is a good approximation for certain range. Hence, the distribution is exponential.
(Right) ($\xi = \Delta x_+, \Delta x_-, \Delta y_+, \Delta y_-$) The distribution appears exponential for $\xi = \Delta y_+$. However it is not clear whether the distribution is power law or exponential in other direction (see figure 2.13 also.)

where $t = pT$, M is total number of tracers, $\Delta \boldsymbol{X}_j^{\mathrm{k}} = \left[\Delta X_j^{\mathrm{k}}, \Delta Y_j^{\mathrm{k}}, \Delta Z_j^{\mathrm{k}}\right]$ is the displacement from j^{th} cycle to $(j+1)^{th}$ cycle, $\boldsymbol{r}^{\mathrm{k}}(p)$ is the total displacement of k^{th} particle. We run the simulations upto ~ 400 cycles. If the tracer particles diffuses through Taylor dispersion [14], then $\langle r^2 \rangle \propto t$. However we see that, the slope of $\langle r^2 \rangle$ in log-log plot is between 1 and 2 (see figure 2.11) but never reaches 1. This may mean super diffusion.

To develop a clear understanding, we calculate the probability distribution function ($\mathcal{P}(\Delta X_j)$) of each component of ΔX_j. We look at the complement of $\mathcal{P}(\Delta X_j)$,

$$\mathcal{Q}(\Delta x_j) = 1 - \int_0^{\Delta x_j} \mathcal{P}(\xi) d\xi, \tag{2.15}$$

where $j = 1, 2, 3$ using rank-order method in figure 2.12 – this method avoids binning error. We separate the positive and negative displacements and compute $\mathcal{Q}(\Delta X_j)$ for each case. We find $\mathcal{Q}(\Delta z)$ has an exponential tail as shown in figure 2.12. However it is not clear whether the tail of $\mathcal{Q}(\Delta Y)$, $\mathcal{Q}(\Delta X)$ fits exponential or power-law (see figure 2.12,2.13). In all of these cases, $\mathcal{Q}(\xi)$ falls off faster than ξ^{-3}, where $\xi = \Delta X, \Delta Y, \Delta Z$.

The $\mathcal{Q}(\Delta s)$, $\Delta s = \sqrt{\Delta X^2 + \Delta Y^2}$, is shown in figure 2.13(Right). The tail of $\mathcal{Q}(\Delta s)$ fits straight-line of slope ~ -3 in log-log plot (figure 2.13(Right)) i.e. $\mathcal{Q}(\Delta s) \propto (\Delta s)^{-3}$. This implies that the second moment of $\mathcal{P}(\Delta s)$ is finite. Using central limit theorem, we say that $\boldsymbol{r}(p)$ must follow normal distribution and $\langle r^2 \rangle \sim t$. Although we do not see $\langle r^2 \rangle \propto t$ with the given data hence can not compute the diffusion coefficient.

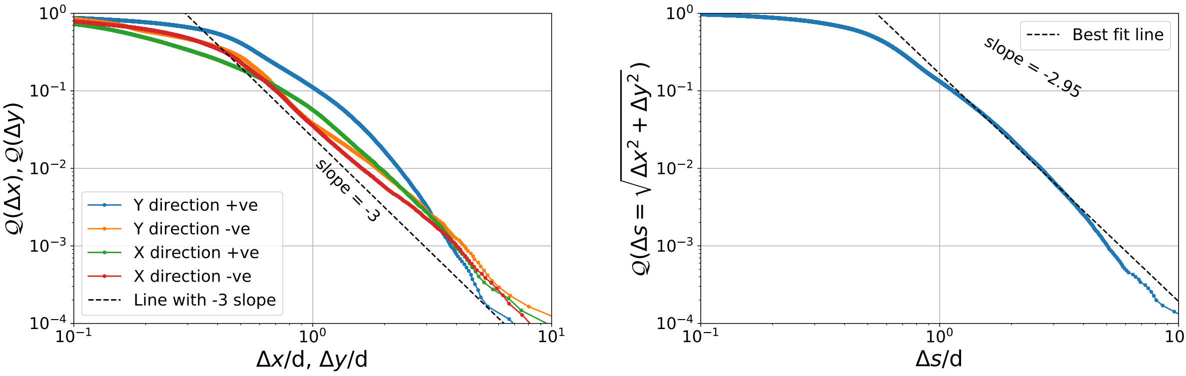

Figure 2.13: Log-log plots of $\mathcal{Q}(\xi)$, where $\xi = \Delta x, \Delta y, \Delta s$. (Left) The distribution falls off faster than $\mathcal{Q}(\xi) \propto \xi^{-3}$ for all cases.
(Right) ($\xi = \Delta s$), where $s = \sqrt{x^2 + y^2}$. Tail of the distribution fits power-law behavior and drops faster than $\mathcal{Q}(\Delta s) \propto \Delta s^{-3}$.

Bibliography

1. Wada, H. & Netz, R. R. Non-equilibrium hydrodynamics of a rotating filament. *EPL (Europhysics Letters)* **75,** 645 (2006).
2. Slowicka, A., Stone, H. A. & Ekiel-Jezewska, M. L. Flexible fibers in shear flow: attracting periodic solutions. *arXiv preprint arXiv:1905.12985* (2019).
3. Chakrabarti, B. *et al.* Flexible filaments buckle into helicoidal shapes in strong compressional flows. *Nature Physics,* 1–6 (2020).
4. Kerswell, R. Recent progress in understanding the transition to turbulence in a pipe. *Nonlinearity* **18,** R17 (2005).
5. Suri, B., Kageorge, L., Grigoriev, R. O. & Schatz, M. F. Capturing turbulent dynamics and statistics in experiments with unstable periodic orbits. *Physical Review Letters* **125,** 064501 (2020).
6. Page, J., Dubief, Y. & Kerswell, R. R. Exact traveling wave solutions in viscoelastic channel flow. *Physical Review Letters* **125,** 154501 (2020).
7. Hopf, E. A mathematical example displaying features of turbulence. *Communications on Pure and Applied Mathematics* **1,** 303–322 (1948).
8. Franco-Gómez, A., Thompson, A. B., Hazel, A. L. & Juel, A. Bubble propagation in Hele-Shaw channels with centred constrictions. *Fluid Dynamics Research* **50,** 021403 (2018).
9. Gaillard, A. *et al.* The life and fate of a bubble in a geometrically perturbed Hele-Shaw channel. *Journal of Fluid Mechanics* **914** (2021).
10. Cvitanovic, P. *et al.* Chaos: classical and quantum. *ChaosBook. org (Niels Bohr Institute, Copenhagen 2005)* **69,** 25 (2005).
11. Knoll, D. A. & Keyes, D. E. Jacobian-free Newton–Krylov methods: a survey of approaches and applications. *Journal of Computational Physics* **193,** 357–397 (2004).
12. Saad, Y. & Schultz, M. H. GMRES: A generalized minimal residual algorithm for solving nonsymmetric linear systems. *SIAM Journal on scientific and statistical computing* **7,** 856–869 (1986).
13. Guennebaud, G., Jacob, B., Avery, P., Bachrach, A., Barthelemy, S., *et al. Eigen v3* 2010.
14. Taylor, G. I. Dispersion of soluble matter in solvent flowing slowly through a tube. *Proceedings of the Royal Society of London. Series A. Mathematical and Physical Sciences* **219,** 186–203 (1953).

Chapter 3

Future work

The work investiagtes the fate of a filament in Stokes flow. However the system is not close to a real microfluidic devices. First step towards it, is to simulate the dynamics of elastic filament in a flow with boundaries.

3.1 Immersed boundary method

The method introduced by Peskin [1], is an efficient way to simulate the boundaries. It treats the boundary as an elastic object. The elastic boundary changes the flow of the fluid and the fluid also moves the boundary simulatneously [2].

3.1.1 Fast multipole method

Time complexity of the hydrodynamic ineteraction between N particles is of $O(N^2)$. While simulating the boundaries using immersed boundary method, N can be very large which slows down the simulation. Similarly, simulation of a long fibre in Stokes flow is also very slow [3]due to high time complexity. Fast multipole method [4, 5] reduces the time complexity upto $O(N\log(N))$ for an average case. Basic idea behind the algorithm is to approximate the solution by ignor the far-field interactions and only deal with near interactions in great detail.

Fast multipole method (FMM) [4, 5] is a technique to deal with general N-body problems with an average time complexity of $O(N\log(N))$. Figure 3.1 shows the comparison of computation time for a filament with N beads (horizontal axis) for FMM and direct computation.

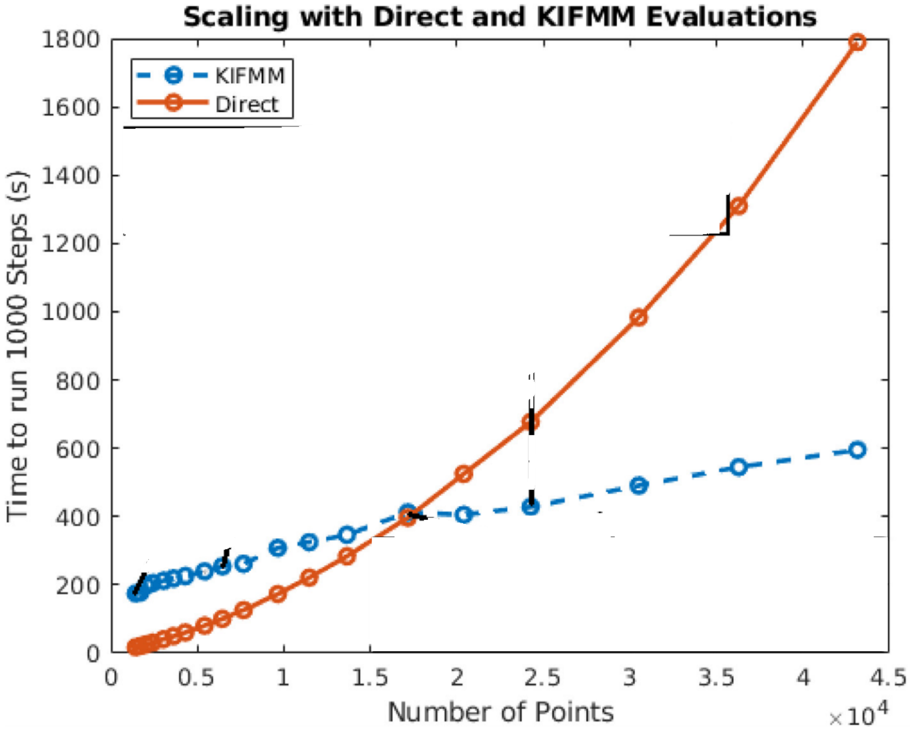

Figure 3.1: Scaling of computation time with kernel independent fast multipole method (KIFMM) ($O(Nlog(N))$) & direct computation ($O(N^2)$). Simulating filament with higher (L/d) ratio (or higher softness) requires more number beads, and FMM is proved to be very useful. Figure adapted and reprinted with permission from LaGrone et. al. [3].

Bibliography

1. Peskin, C. S. Flow patterns around heart valves: a numerical method. *Journal of computational physics* **10,** 252–271 (1972).
2. Bringley, T. T. & Peskin, C. S. Validation of a simple method for representing spheres and slender bodies in an immersed boundary method for Stokes flow on an unbounded domain. *Journal of Computational Physics* **227,** 5397–5425 (2008).
3. LaGrone, J., Cortez, R., Yan, W. & Fauci, L. Complex dynamics of long, flexible fibers in shear. *Journal of Non-Newtonian Fluid Mechanics* **269,** 73–81 (2019).
4. Rokhlin, V. Rapid solution of integral equations of classical potential theory. *Journal of computational physics* **60,** 187–207 (1985).
5. Greengard, L. & Rokhlin, V. *A fast algorithm for particle simulations.* tech. rep. (YALE UNIV NEW HAVEN CT DEPT OF COMPUTER SCIENCE, 1986).

Appendix A

Non-linearity of Euler elastica

A.1 Euler equation: a static problem

There are two ways to obtain an equilibrium configuration of the filament. First, we write the equation of force-balance and moment-balance on every element of the filament [1]. Second, we can use variational principle to minimize the Hamiltonian to get the equilibrium configuration of the filament [2]. We take the second approach to describe the dynamics of the filament.

Let us ignore the twist of the filament and concentrate only on the bending forces. Consider a macroscopic filament with force per unit length given as $Q(s)$. For the equilibrium configuration of the filament $\boldsymbol{R}(s)$ we write:

$$\boldsymbol{q}(s) = -\frac{\delta\mathcal{H}\left(\boldsymbol{R}''\right)}{\delta\boldsymbol{R}} = \frac{d^2}{ds^2}\left(\frac{\partial\mathcal{H}\left(\boldsymbol{R}''\right)}{\partial\boldsymbol{R}''}\right) = \frac{d^2}{ds^2}\left(-B\frac{d^2\boldsymbol{R}(s)}{ds^2}\right) = -B\frac{d^4\boldsymbol{R}(s)}{ds^4} \tag{A.1}$$

where $\frac{\delta(\cdot)}{\delta\boldsymbol{R}}$ denotes the functional derivative with respect to $\boldsymbol{R}$.

Equation A.1 is the famous Euler-Bernoulli beam equation [3]. The last simplification is valid only when B does not change with arc-length coordinate,s. Equation A.1 describes the configuration of filament at equilibrium. Let us consider the forces that acts on discrete points. We can either implement it in the boundary condition or incorporate in the equation. Let us take:

$$\int_{s=0}^{L}\boldsymbol{q}(s)ds = \sum_{i\ \epsilon\ \text{forces}}\boldsymbol{F}_i = \boldsymbol{F} = F_1\hat{\boldsymbol{d}}_1 + F_2\hat{\boldsymbol{d}}_2 + F_3\hat{\boldsymbol{d}}_3 \tag{A.2}$$

where $\boldsymbol{F}$ is the summation over all the forces acting on the filament. As described earlier, we take $\hat{\boldsymbol{d}}_3$ along $\widehat{\boldsymbol{T}}$.

At equilibrium, force acting along the tangent can not bend a filament. So we do not write equations in that direction. We write down the equation in the other two direction by integrating both sides of equation A.1: e

$$-B\frac{d^3\boldsymbol{R}(s)}{ds^3}\cdot\hat{\boldsymbol{d}}_i = \boldsymbol{F}\cdot\hat{\boldsymbol{d}}_i \quad ; \quad \mathrm{i} = 1,2 \tag{A.3a}$$

This can also be written as following:

$$B\frac{d\boldsymbol{R}(s)}{ds} \times \frac{d^3\boldsymbol{R}(s)}{ds^3} = \boldsymbol{F} \times \frac{d\boldsymbol{R}(s)}{ds} \tag{A.3b}$$

where $\hat{\boldsymbol{d}}_3 = \frac{d\boldsymbol{R}(s)}{ds}$

Note that, the equation is converted to a third order differential equation now.

A.1.1 Euler Elastica for inextensible filaments:

Here we consider inextensible filaments. The in-extensibility constraint arises naturally for the filaments as discussed in section **??** where viscous forces are dominant as we shall see later in section 1.3.2. The local in-extensibility constraint reads as:

$$\sqrt{\frac{d\boldsymbol{R}(s)}{ds} \cdot \frac{d\boldsymbol{R}(s)}{ds}} = 1 \tag{A.4}$$

We use the method of Lagrange multiplier to impose the constraint [4].

$$\mathcal{H}_{\text{tot}} = \mathcal{H} + \int_0^L \Lambda(s) \left(1 - \sqrt{\frac{d\boldsymbol{R}(s)}{ds} \cdot \frac{d\boldsymbol{R}(s)}{ds}}\right) \tag{A.5}$$

where $\Lambda(s)$ is the Lagrange multiplier. Variation of equation A.5 gives the in-extensibility constraint.

$$B\frac{d^4\boldsymbol{R}(s)}{ds^4} - \frac{d}{ds}\left(\Lambda(s)\frac{d\boldsymbol{R}(s)}{ds}\right) + \boldsymbol{Q}(s) = 0 \tag{A.6}$$

We see that there is an additional force term in the, $\hat{\boldsymbol{d}}_3 = \widehat{\boldsymbol{T}}$, direction due to constraint. This is expected as the stretching/compressing should induce tension along the filament. Physically $\Lambda(s)$ is the magnitude of the force along the filament, which is analogous to the tension in the filament arising from internal stresses. Since the tension always acts in $\hat{\boldsymbol{d}}_3$ direction, equation A.3b is still valid in $\hat{\boldsymbol{d}}_1(s)$ or $\hat{\boldsymbol{d}}_2(s)$ direction.

For a better physical understanding, consider a filament stretched at both ends by equal and opposite force $|P|$. Tension in the filament is equal to the force $|P|$. Equation A.6 becomes [1]:

$$B\frac{d^4\boldsymbol{R}(s)}{ds^4} - |P|\frac{d^2\boldsymbol{R}(s)}{ds^2} + \boldsymbol{Q}(s) = 0 \tag{A.7}$$

Equation A.7 can be integrated to give equation for the concentrated forces as in equation A.3b.

The form of Euler-Bernoulli equation (A.1,A.7) is deceiving, as it is linear in arc-length coordinate s, although dependence of s on extrinsic coordinate system may be non-linear which makes the Euler Elastica a non-linear problem. The Euler Elastica simplifies to a linear problem for small deformations.

A.1.2 Small deformations:

Consider a straight filament (zero twist and curvature and circular cross-section) embedded in two-dimensional space which is clamped at one end, but free at the other end (figure A.1). A constant force is applied at the free-end of the filament. In the case of small deformation, the tangent vector, $\widehat{\boldsymbol{T}}$, varies very slowly along the filament. For a Cartesian coordinate system, if we take the tangent along the z-axis i.e. $\widehat{\boldsymbol{T}} \approx \hat{z}$. The arc-length of the filament $s \approx z$, where z is the length along z-axis, from the origin [1]. The small deflection in x direction is $X(z)$. Equation A.7 is simplified to give the following relation:

$$B\frac{d^4X(z)}{dz^4} - |T|\frac{d^2X(z)}{dz^2} + Q_x(s) = 0 \tag{A.8}$$

where $|T|$ is the tension in the filament and q_x is the external force per unit length in x direction. The tension, T, in the filament is proportional to the extension in the filament, ΔL [1]. For small deformation, extension in the filament reads as:

$$\Delta L = \int_0^L \left(\sqrt{1+\left(\frac{dX(z)}{dz}\right)^2} - 1\right) dz \tag{A.9a}$$

$$\Delta L \approx \frac{1}{2}\int_0^L \left(\frac{dX(z)}{dz}\right)^2 dz \tag{A.9b}$$

$$T \approx \frac{ES}{2L}\int_0^L \left(\frac{dX(z)}{dz}\right)^2 dz \tag{A.9c}$$

Last relation is written assuming the linear constitutive stress-strain relation. Where Y is the Young's modulus, $S \sim d^2$ is the cross-sectional area, d is the cross-sectional diameter of the filament. Note that, T in equation is not known a priori but it is a parameter which is calculated using equation A.9 to give the relation between known quantities and T.

Dimensional estimates for $T(s)$ using equation A.9 gives us $T \sim ES\left(\frac{\delta}{L}\right)^2$ (where δ is the deformation). The first and second term in equation A.8 is:

$$B\frac{d^4X(z)}{dz^4} \sim Ed^4\frac{\delta}{L^4}, \qquad T\frac{d^2X(z)}{dz^2} \sim Ed^2\left(\frac{\delta^3}{L^4}\right) \tag{A.10}$$

Both terms are comparable if $\delta \sim d$. So for $\delta << d$, equation A.8 converts to:

$$B\frac{d^4X(z)}{dz^4} + q_x(s) = 0 \tag{A.11}$$

The Elastica problem simplifies to a linear equation (A.11) for the limit of small deformation. We now have two linear equtions (A.8, A.11) in the limit of small deformation. Equation A.11 is strictly valid iff the deformation,$\delta << d$. Equation *A.8* is more suitable if $\delta \sim d \ll L$.

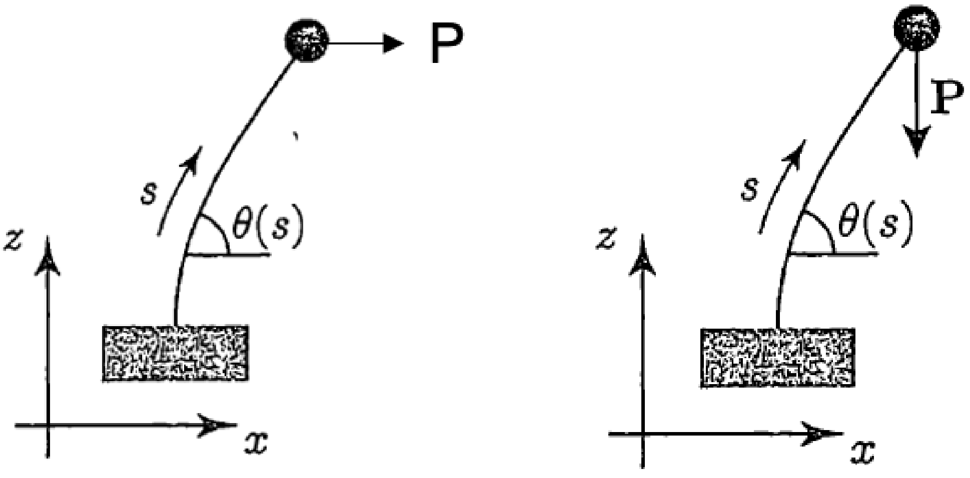

(a)

(b)

Figure A.1: Filament clamped at one end (origin, $s = 0$) but free at other end. A constant force is applied on the free-end in x for (a), and in z direction for (b). Figure adapted from [2] but redrawn.

We consider two examples as shown in figure A.1. In both cases, the filament is clamped at the bottom and free at the other end. At the clamped end (origin), we have $X(z = 0) = \frac{dX}{dz}(z = 0) = 0$, and at the free end, we have $\frac{d^2X}{dz^2}(z = L) = 0$, where L is the length of the filament. The angle that the filament makes with x-axis is represented as $\theta(s)$.

Let us consider both the cases in the limit of small deformation, $\delta << L$. In the figure (A.1(a)), the load is acting in the transverse direction. Since there is no force in $\hat{\boldsymbol{d}}_3 = \widehat{\boldsymbol{T}} \approx \hat{z}$ direction, we integrate the equation A.8 once, and take a cross product with $\hat{\boldsymbol{d}}_3$., i.e. :

$$F_x = -B\frac{d^3X(z)}{dz^3} = P \tag{A.12}$$

Note that, A.12 is similar to A.11 but they are derived under different assumptions. We get:

$$X(z) = -\frac{Pz^2}{6B}(z - 3\ell) \tag{A.13}$$

In the second case, the force is applied in the negative z direction. Since there is a force component in $\hat{\boldsymbol{d}}_3 = z$ direction for this case, we solve equation A.7 to get the solution. Let us further assume, $\delta << d$ (δ is the deformation), we use equation A.11 to find out that the straight filament, $X(z) = 0$, is the only solution.

Now we allow higher deformation such that $\delta \sim d << L$, equation A.11 is not applicable anymore. We use equation A.8 ($Q_x = 0$) to get the solution. We already know that the system has trivial solution ($X(z) = 0$) for small deformation i.e. for small forces, $P < P_{cr}$. For $P < P_{cr}$, the rod is stable for any small perturbations. At $P > P_{cr}$, the rod still has trivial solution, but is unstable for any perturbation, which results in large bending of the rod. At $P = P_{cr}$, the straight rod is in neutral equilibrium with the bent rod. So the bent filament satisfies the equation of large deflection (A.1) as the approximation $\delta << L$ does not hold anymore. Though, we can get the value of $P_{cr}$by solving linear Euler-Bernoulli equation. Since the rod is in neutral equilibrium at $P = P_{cr}$, the rod has solutions other than the trivial solution. So the critical force P_{cr} is the value of P for which the equation A.8 (with $Q_x = 0$) have non-zero solution.

For this particular example (figure A.1), we solve equation A.8 with appropriate boundary conditions to get:

$$P_{cr} = \frac{\pi^2 B}{4\ell^2} \tag{A.14}$$

For $P = P_{cr}$, the rod has three solutions which exist simultaneously.

A.1.3 Non-linearity of the Euler Elastica:

Let us solve the problem, shown in figure A.1(b), for the case of large deformation. In Cartesian coordinates, the tangent vector of the filament is given as [2]:

$$\widehat{\boldsymbol{T}}(\theta(s)) = \frac{d\boldsymbol{R}(s)}{ds} = \frac{d(x(s)\boldsymbol{e}_x + z(s)\boldsymbol{e}_z)}{ds} = \cos\left[\theta(s)\right]\boldsymbol{e}_x + \sin\left[\theta(s)\right]\boldsymbol{e}_z \tag{A.15}$$

where $\theta(s)$ is the angle, that tangent to the filament at any point s makes with the x-axis as shown in figure A.1(b). It varies with the arc-length coordinate (s), where s goes from 0 to ℓ from clamped end to the free end.

We simplify equation A.3b using the given force $\boldsymbol{F} = -P\boldsymbol{e}_z$ and equation A.15. (There will be contribution from tension in the filament in the direction $\hat{\boldsymbol{d}}_3$ but this does not change equation A.3b) Which gives us the following relation:

$$B\frac{d^2\theta(s)}{ds^2} - P\cos\bigl(\theta(s)\bigr) = 0 \tag{A.16}$$

For small deformation, $\theta(s) \to \frac{\pi}{2}$. A variable change of $\psi(s) = \theta(s) - \frac{\pi}{2}$ means $\psi(s) \to 0$ for small deformations. Equation A.16 reads as:

$$B\frac{d^2\psi(s)}{ds^2} + P\sin\bigl(\psi(s)\bigr) = 0 \tag{A.17}$$

This equation is solved with boundary condition:

$$\psi(0) = 0, \qquad \left.\frac{\mathrm{d}\psi}{\mathrm{ds}}\right|_{\ell} = \psi'(\ell) = 0 \tag{A.18}$$

Equation A.17 is non-linear in $\psi(s)$. Although for small deformation, the equation A.17 is converted to a linear equation, as discussed above ($s \approx z$, $\sin\bigl(\psi(s)\bigr) \approx \psi(s)$).

Equation A.17 is integrated to give the following:

$$\frac{B}{2}\left(\frac{d\psi(s)}{ds}\right)^2 - P\cos\bigl(\psi(s)\bigr) = C' \tag{A.19}$$

We use the boundary condition, $\psi'(\ell) = 0$, to get $C' = -P\cos\psi(L)$. Introduce $\ell^* = \sqrt{B/2P}$, $\bar{\ell} = \ell/\ell^*$, $\bar{s} = s/\ell^*$ and we get:

$$\bar{s} = \frac{1}{\ell^*}\int_0^s \mathrm{d}\sigma = \int_0^\psi \frac{\mathrm{d}\phi}{\sqrt{\bigl(\cos(\phi) - \cos(\psi_{\mathrm{L}})\bigr)}} \tag{A.20a}$$

$$\bar{s} = \sqrt{2}\boldsymbol{\mathcal{S}}(\frac{\psi_{\bar{\ell}}}{2})\mathcal{F}\left(\frac{\psi}{2}\middle|\csc\left(\frac{\psi_{\bar{\ell}}}{2}\right)^2\right) = \mathcal{Q}(\psi(\bar{s}), \psi(\bar{\ell})) \tag{A.20b}$$

where $\mathcal{F}(\psi/2|\csc\bigl(\psi/2\bigr)^2)$ is the incomplete elliptic integral of first kind [5]. Note that, $\psi(s) = 0$ is always one of the solutions of the equation A.19, although we disregard this solution while inverting it to get equation A.20a. We use the condition of in-extensibility to determine the value of $\psi(\bar{\ell})$ using equation A.20b.

For the critical $\bar{\ell}_{cr}$ or P_{cr}, we should take the limit $\psi_{\bar{\ell}} \to 0$ i.e. :

$$\bar{\ell}_{cr} = \lim_{\psi(\bar{\ell})\to 0} \mathcal{Q}(\psi(\bar{\ell}), \psi(\bar{\ell})) = \frac{\pi}{\sqrt{2}} \tag{A.21}$$

If force $P < \frac{B\pi^2}{4}$ or $\bar{\ell} < \bar{\ell}_{cr}$, equation A.20b has no solution, but we already know one solution of the system, $\psi(s) = 0$, i.e. the straight compressed filament. As we increase the force, $P > \frac{B\pi^2}{4}$, we get two other non-trivial solutions, which are symmetric under the change of sign $\psi(s)$ i.e. the filament can buckle in either direction. In a practical system, it depends upon the imperfections in the filament. Any initial noise in any direction leads the filament to find equilibrium in that direction. For large enough force, all three solution exist simultaneously in two-dimensional system for the given set of boundary condition.

If the force P is just larger than $\frac{B\pi^2}{4}$ i.e. $P - \frac{B\pi^2}{4} \to \epsilon^+$ $(\epsilon \to 0)$ we Taylor expand $\mathcal{Q}$ to get higher order terms. This gives us:

$$\psi(s) \approx \psi(\bar{\ell})\sin\left(\frac{\pi s}{2L}\right) \tag{A.22}$$

Bibliography

1. Landau, L. & Lifshitz, E. Theory of Elasticity,(Pergamon Press, Oxford, 1986).
2. Audoly, B. & Pomeau, Y. in *Peyresq Lectures On Nonlinear Phenomena* 1–35 (World Scientific, 2000).
3. Gere, J. & Timoshenko, S. Mechanics of materials, 1997. *PWS-KENT Publishing Company, ISBN 0* **534,** 4 (1997).
4. Goldstein, R. E. & Langer, S. A. Nonlinear dynamics of stiff polymers. *Physical review letters* **75,** 1094 (1995).
5. Gradshteyn, I. S. & Ryzhik, I. M. *Table of integrals, series, and products* (Academic press, 2014).